Near-Surface Shear-Wave Velocity Measurements in Unlithified Sediment

by

Benjamin Thomas Rickards
B.S., Trinity University, 2006

Submitted to the Department of Geology
and the Faculty of the Graduate School of the University of Kansas
in partial fulfillment of the requirements for the degree of
Master of Science
2011

Advisory Committee:

Don W. Steeples, Chair

Richard D. Miller

Jennifer A. Roberts

Luis A. Gonzalez
for the Department

Date Defended: 12/16/2011

The Thesis Committee for Benjamin Thomas Rickards certifies that
this is the approved version of the following thesis:

Near-Surface Shear-Wave Velocity Measurements in Unlithified Sediment

Advisory Committee:

Don W. Steeples, Chair

Richard D. Miller

Jennifer A. Roberts

Luis A. Gonzalez
for the Department

Date Approved: 12/16/2011

Abstract

Shear-wave (S-wave) velocity can be directly correlated to material stiffness making it a valuable physical property that has found uses in construction, engineering, and environmental projects. This study compares three different methods, Multichannel Analysis of Surface Waves (MASW), S-wave tomography, and downhole seismic for measuring S-wave velocities, investigates and identifies the differences among the methods' results, and prioritizes the different methods for S-wave use at the U. S. Army's Yuma Proving Grounds (YPG) north of Yuma, AZ. A large signal-to-noise ratio and a layered depositional architecture at the study site gives the MASW method much potential, but higher-mode energy resulting from velocity discontinuities reduces the effectiveness of the method shallower than 20 ft. First arrival analysis provides evidence of a velocity discontinuity within the first 10 feet of unconsolidated sediment. S-wave first arrivals were picked using impulsive sledgehammer data which were then used for both tomographic inversion and refraction analysis. Three-component downhole seismic data were collected by using a locking geophone coupled with the borehole casing to estimate seismic velocities directly. This study helps to identify the strengths and weaknesses of each of these methods at sites similar to YPG. MASW results show a low-velocity layer at a depth of about 50 feet that is verified by downhole seismic data and is undetectable through traditional refraction tomography. However S-wave refraction tomography provides more convincing results at shallow depths where the MASW method fails. Using both methods in an integrated fashion provide the most accurate depiction of S-wave velocity characteristics in the shallow unconsolidated sediments at YPG.

Acknowledgements

First I would like to thank my family and friends for all of their support. I would like to thank the faculty of the department, and the Kansas Geological Survey, most especially Don Steeples and Rick Miller for their patience and believing in my ability, as well as for their financial support and academic advice. I am grateful to the US Army Engineer Research & Development Center and the Kansas Geological Survey for allowing the use of this data. I appreciate Owen Metheny, Brett Wedel, Tony Wedel, Joe Anderson, Joe Kearns, and Shelby Peterie for helping collect the data. Special thanks go to Shelby Peterie, Julian Ivanov, and Janghai Xia for all their help in learning these data processing methods. Finally, thanks to Kathryn Hoffmeister for her revisions and her support.

Table of Contents

List of Figures

Introduction

Over the past 20 years, information gleaned from shallow seismic S-wave velocities has become more available for use in disciplines ranging from environmental geophysics to civil engineering. A variety of geophysical techniques has been developed to determine S-wave velocities and each method has its strengths and weaknesses in various geologic settings. The purpose of this research is to determine the most accurate method for determining near-surface S-wave velocities for unconsolidated sediments within the U.S. Army's Yuma Proving Grounds, Arizona.

Seismic-wave velocities in rocks are directly related to their physical properties and are used to provide valuable insights about the rock's mechanical and petrologic properties (Grant and West, 1965). Compressional waves (P-waves) propagate by changing the rock's volume, while S-waves distort the rock matrix, leaving the volume unchanged (Helbig, 1986). When the deformation is entirely elastic the stress applied to a body is proportional to the resulting strain, the ratio of stress to strain is called the modulus. Moduli are somewhat analogous to the spring constant in Hooke's law where a force acting on a spring causes it to compress or expand:

$$F = -sx \tag{1}$$

Here, F is the restoring force, s is the spring constant, and x is the resulting displacement from equilibrium. As long as the deformation is elastic (Figure 1), the displacement of the spring is proportional to the force applied to it by a factor of s. The two principal moduli of interest in seismology when discussing velocity are the bulk modulus, k, and the shear modulus, μ:

$$k = V\frac{\Delta P}{\Delta V} \qquad\qquad \mu = \frac{\Delta Stress_{shear}}{\Delta Strain_{shear}} \qquad \textbf{(2,3)}$$

Here, V is volume, and P is pressure. P-wave velocities vary with changes in the bulk modulus, shear modulus, and density, while S-wave velocity changes depend only on the shear modulus and density (Sheriff, 1991):

$$V_P = \sqrt{\frac{\mu + \frac{4}{3}k}{\rho}} \qquad\qquad V_S = \sqrt{\frac{\mu}{\rho}} \qquad \textbf{(4, 5)}$$

Here, V_P is P-wave velocity, V_S is S-wave velocity and ρ is density. The fact that S-wave velocity is independent of a material's compressibility allows for direct comparison to the material's stiffness. Because of this correlation, S-wave velocity measurements are useful for investigating the mechanical-strength properties of the near surface materials.

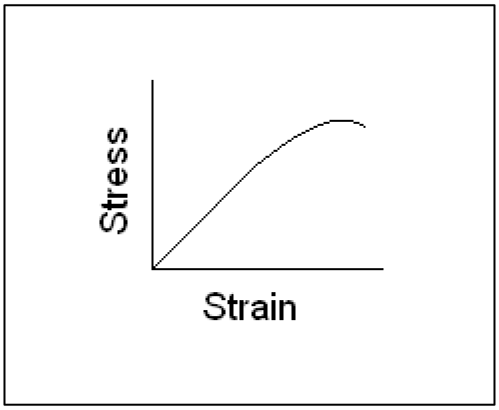

Figure 1: Once the stress-strain relationship becomes non-linear, plastic deformation occurs and potential energy is not entirely conserved.

Recent catastrophic earthquakes in China, Haiti and Japan have underscored the urgency to minimize damage by proper selection of building sites (Anbazhagan and Sithram, 2008) and construction practices. The International Building Code has standardized characterizing earthquake risk with the V_S^{30} rating system which is the average S-wave velocity in the shallowest 30 meters of the subsurface. Studies have linked low S-wave velocities in surface sediments overlying bedrock with relative amplification of ground motion during earthquakes (Borcherdt, 1994). For example, the V_S^{30} system would rank an area with an average S-wave velocity of 600 ft/sec in the top 30 meters as having a relatively high risk for amplifying destructive earthquake waves (Hunter *et al.*, 2010). S-wave studies have also been used to identify subsidence and liquefaction risks for wind-turbine installation (Park and Miller, 2005), investigate potential for levee failure (Ivanov *et al.*, 2006a) and identify subsidence risks from dissolution features (Miller *et al.*, 2009).

One of the first geophysical methods used to characterize the subsurface as early as the 1920's was the P-wave refraction method (Green, 1974). This method assumes that the first coherent wavelet recorded on a trace traveled the highest velocity path from source to receiver. It can be generated either by a wavefront arriving directly from the seismic source, or by energy refracted at depth by a velocity contrast, usually associated with an interface between a change in material (Figure 2A). Refraction tomography, an extension of the refraction method, has become more popular as computer power has increased, (Stewart, 1991).

With diving-wave tomography first-arrival travel times are used in a similar fashion to a traditional refraction survey, however the ray paths are expected to bend without necessarily following a discrete refracting interface (Figure 2B). Next, a generalized initial velocity model of the subsurface is estimated and divided into discrete cells. A refraction survey is then simulated with survey parameters mimicking the dataset that was used to pick the measured first arrivals, populating each cell with a travel time based on that cell's velocity. From each simulated receiver, the path back to the source with the shortest travel time is retraced, this is called a ray path. The calculated travel time from the model is compared with the observed travel time from the real data, and the velocities along the ray path are updated in the next iteration to minimize the difference in ray path travel time. This process occurs over several iterations and is intended to converge on a model that accurately represents the subsurface (Vidale, 1998).

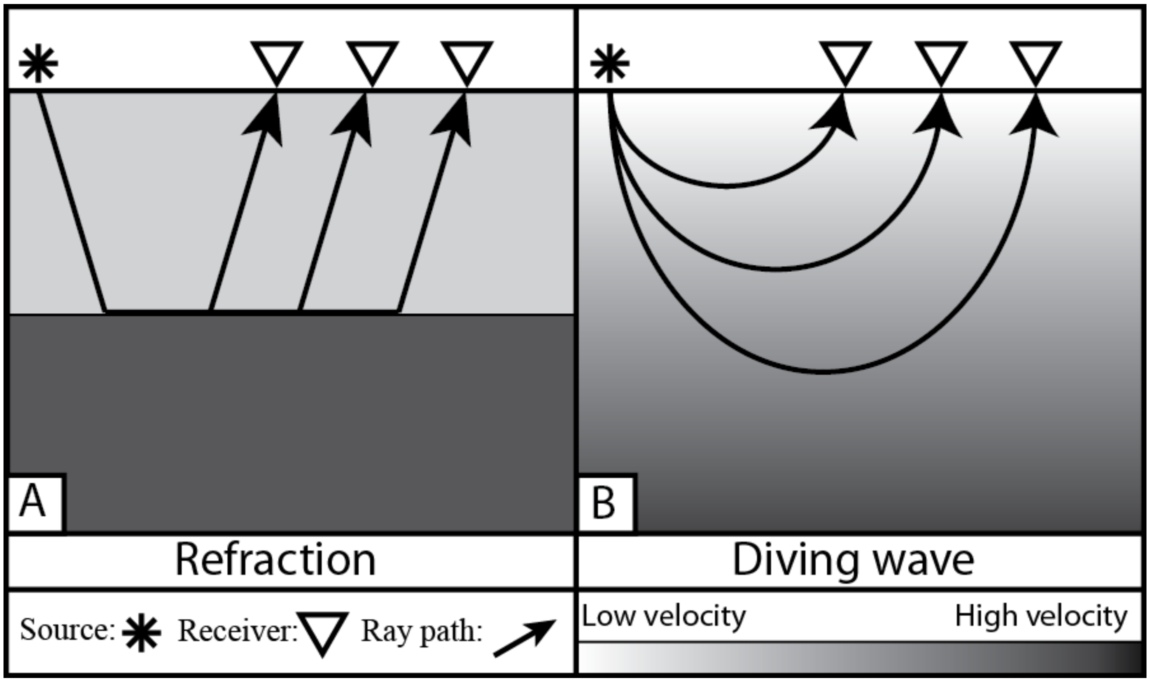

Figure 2: Depiction of velocity structures resulting in refracted first arrivals (A) and diving-wave first arrivals (B). In the refraction case, the velocity increases stepwise with depth, while the diving wave scenario assumes a linearly increasing velocity function.

The primary reason S-wave refraction tomography is a viable method in this study is that diving-wave tomography can be used in a geologic setting like at the YPG where impedance contrasts in the subsurface are not large enough to image within the depths of interest using reflection seismology (Figure 3). A walkaway S-wave survey was conducted at the field site and no reflections in the upper 150 ft were detected.

S-wave tomography works exactly the same way as P-wave tomography, except S-wave tomography uses S-wave first arrival times which are normally not the first arriving energy on a seismogram. With up to 800 ft of receiver offset, the depth of investigation can be estimated down to 200 ft using a rule-of-thumb that the depth of investigation is approximately one-quarter of the spread length (Palmer, 1981). Some potential difficulties with using S-wave tomography include misidentifying S-wave first arrivals and converging to a non-unique solution during the inversion process.

In the past 20 years, surface waves, a component of the wavefield typically regarded as noise by petroleum geophysicists, have become extremely useful for estimating shallow S-wave velocities (Stokoe and Nazarian., 1983). There are two types of surface waves, Love waves, and Rayleigh waves. Rayleigh waves are a result of constructive interference between P- and S-waves reflected from the free-surface boundary (Ewing *et al.*, 1959). This interference pattern results in a wavefront with retrograde-elliptical particle motion that propagates radially from the source, but within half of a wavelength from the surface. In the case where velocity increases with depth discretely, each frequency component of the Rayleigh wave has a unique phase velocity. The phase velocity of a given frequency component of the Rayleigh wave is determined by the thickness of the layer in which it propagates, as well as the P-wave velocity, S-wave velocity and the density of that layer. By measuring the phase velocity for each frequency and holding the rest of these values constant (Xia *et al.* 1999) S-wave velocities can be solved through the process of inversion.

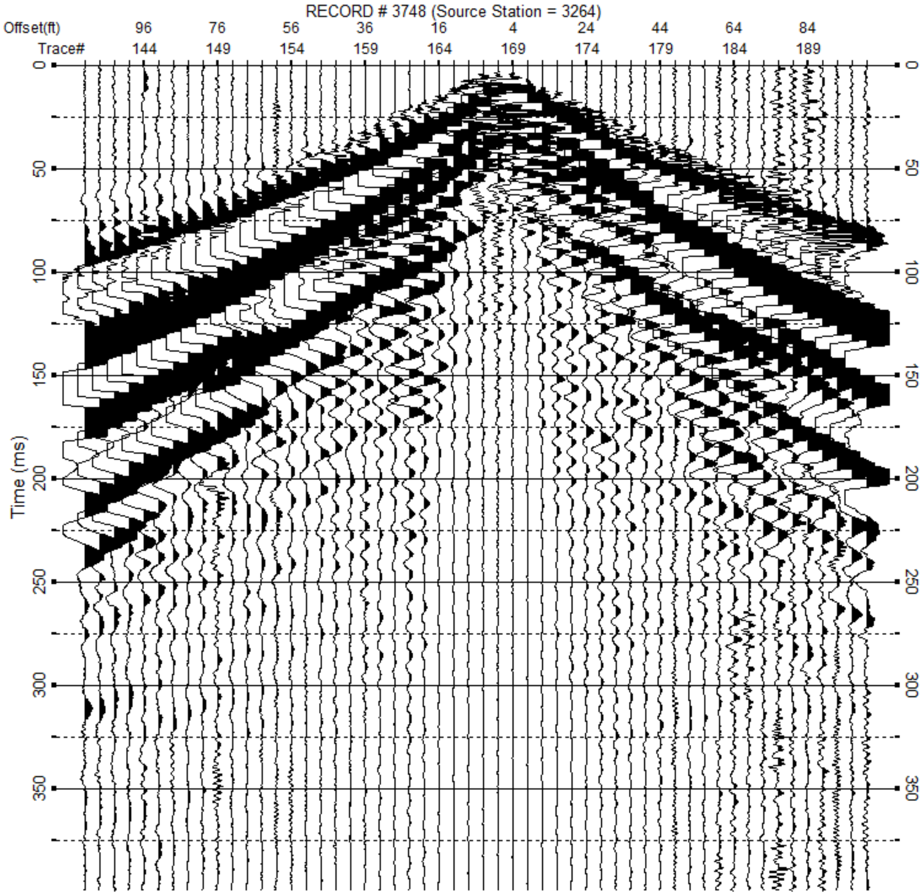

Figure 3: Example of a raw shot gather generated with a shear block and sledgehammer, collected with horizontal geophones oriented parallel with the long axis of the shear block. Due to the lack of useable reflection information within the depth of interest, MASW and S-wave tomography were chosen as the primary methods for this project.

In this thesis, both surface wave inversion and refraction tomography methods are tested against the results of two downhole seismic surveys. A downhole seismic survey can be used to calculate velocity of material between a receiver at depth and a source near the surface of the borehole. The concept of a downhole seismic survey is much simpler and measurement accuracy generally better than either MASW or tomography, and is generally assumed to provide “ground truth” for correlating with other surface geophysical surveys (Crice, 2011). Unfortunately this assertion is based on some assumptions that do not always hold true. These sources of error will be discussed later. Comparison of the results of the downhole seismic surveys with the results from MASW and tomography provide insight into the quality of results from each method.

Geologic Background: Yuma Proving Grounds

The data used in this project were collected at a site at the Yuma Proving Grounds (YPG) within a valley south of the Trigo Peaks mountain range in Southwestern Arizona (Figure 4). The data collection site is located where the distal edge of a modern alluvial fan grades into alluvial plain sediments (Figure 5)(McDonald *et al.*, 2009). These sediments are likely to have been transported predominantly by gravity flow, based on the volcanic nature of the surrounding mountains (Eberly and Stanly, 1978), abundance of fine grained material (Miller *et al.* 2010) and the persistent regional arid climate (Reading, 1996).

Part of the scope of work detailed for the Kansas Geological Survey at the YPG entailed drilling a number of boreholes for sampling purposes. Sampling success in each borehole was somewhat variable due to the combination of very fine sediment, the dry conditions, and the sonic drilling technique in these very dry conditions. However, the on-site geologist was able to evaluate the lithology of the samples that were recovered (Miller *et al.*, 2010). A lithochart was created based on the sampling report, only two wells were successfully sampled beyond 40 ft (Figure 6). In general the materials varied significantly within the upper 40 ft. Materials were classified by variations of clay content, the remainder of the clastic material ranged from silt to gravel. The most notable features in the upper 40 feet were infrequent sand lenses. Beyond 50 feet clay content increased significantly. This material consisted of coarsening upward, poorly sorted subrounded to subangular sediments ranging from gravel to clay (Miller *et al*., 2010).

Modern depositional processes that have shaped the topography of Southwestern Arizona are characteristic of regional block faulting (Reading, 1996). After the decline of the Laramide orogeny, between 53 and 26 million years ago, subaerial fanglomerates and associated lake beds were deposited within topographic lows on older bedrock surfaces in southwestern Arizona. At the end of this period, magmatism increased dramatically, causing regional heating of the crust, plutonism, and minor mineralization. Volcanic tuffs and breccia flows altered the previously established drainage systems, shifting the depositional patterns. Sediments deposited during this time are mostly of lacustrine and fluvial origin and are intercalated with volcanic extrusions. This period of tectonism is known as the Mid-Tertiary orogeny (Eberly and Stanley, 1978).

After the Mid-Tertiary Orogeny began to slow, relative sea level fall created an expansive unconformity around 17 million years ago. Volcanic activity and fanglomerate deposition continued as before, but this time was accompanied by regional extension. Regional block faulting began in the late Miocene, which created the structures that now dominate the present day topography. Horst-and-graben development altered the previous drainage patterns, allowing sediment shed directly from horsts to be deposited in adjacent grabens, leaving each basin with unique depositional environments. Around 10 to 6 million years ago, faulting began to wane, and smaller basins began to coalesce allowing exterior drainage systems to develop (Eberly and Stanley, 1978).

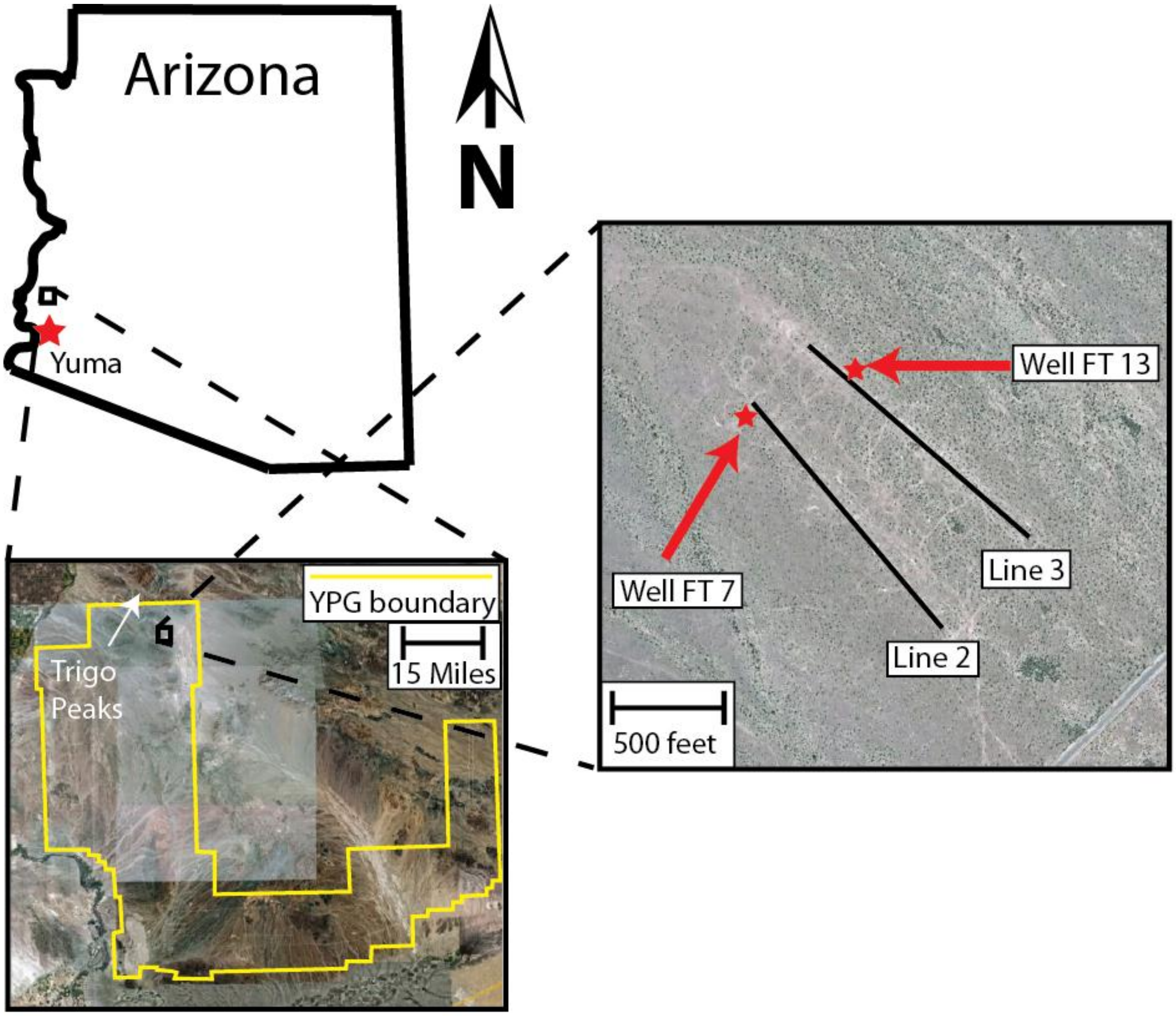

Figure 4: Location map describing geographic area of the survey and layout of seismic lines as well as borehole positions. Station numbers increase to the northwest. Images are from Google maps.

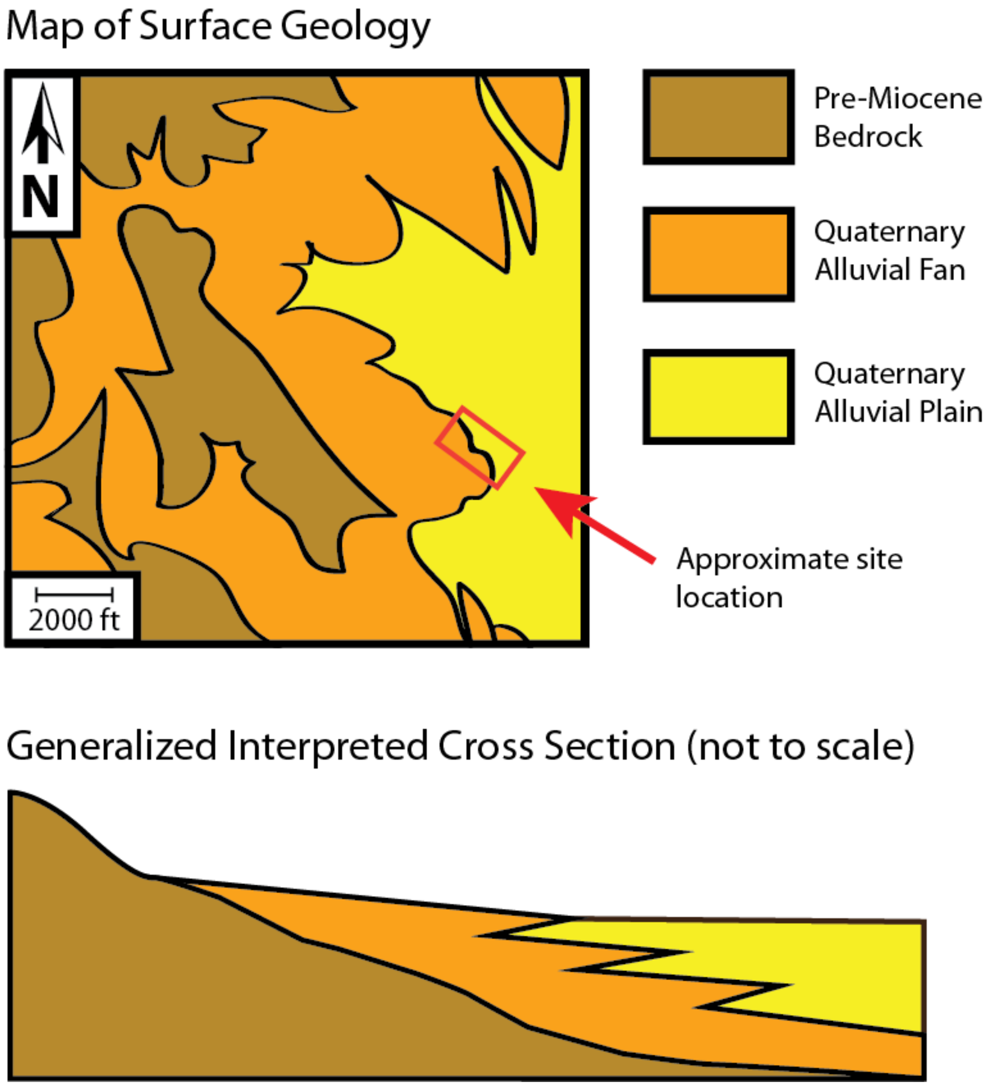

Figure 5: Figure representing surface geology after McDonald *et al*., (2009) and interpreted generalized cross section suggesting stratigraphic relationships between the facies listed here (not to scale). The YPG site is located where the distal portion of an alluvial fan grades into alluvial terrace.

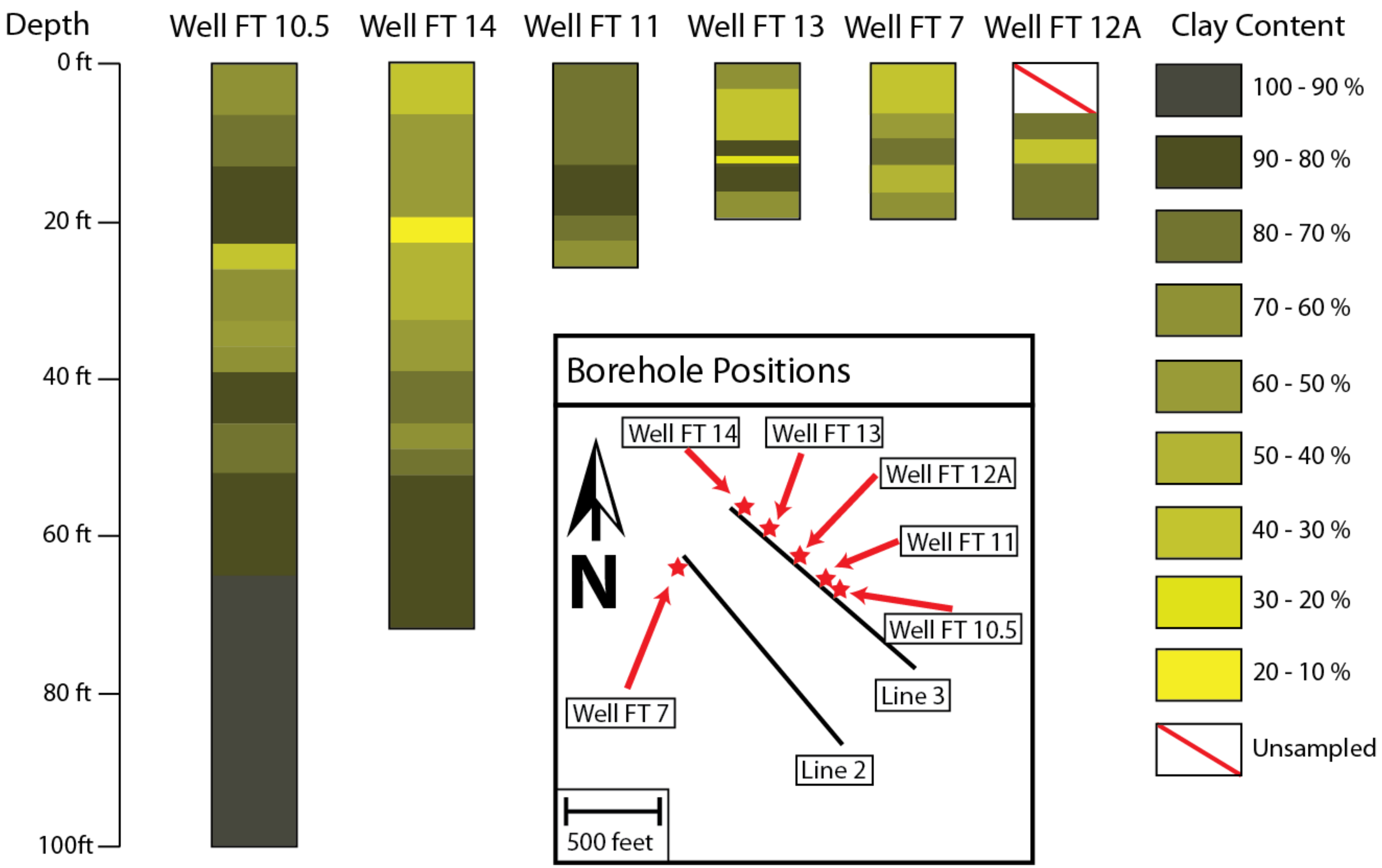

Figure 6: Lithochart describing sediments sampled from wells drilled at the site of the survey.

Multichannel Analysis of Surface Waves

Introduction

The MASW method estimates S-wave velocities by exploiting the dispersive nature of Rayleigh waves through mathematical inversion (Park *et al.*, 1999; Xia *et al*. 1999). Rayleigh waves are the result of the combination of evanescent P- and vertical S-waves in the vicinity of a free surface-boundary (Ewing *et al.*, 1959). Because these waves only exist within close proximity to the free surface, they cannot propagate spherically as body waves do. The vast majority of energy from Rayleigh waves only penetrates to depths of about one half of a wavelength.

In a typical geologic setting, velocity increases with depth. If this is the case Rayleigh waves with long wavelengths propagate through deeper layers with higher velocities, while high frequencies are confined to the shallower layers with relatively low velocities. This makes the Rayleigh wave dispersive (Babuska and Cara, 1991). According to Xia *et al*. (1999), the S-wave velocity of each layer is the most sensitive parameter controlling the phase velocities of the Rayleigh wave. This allows dispersive Rayleigh waves to be exploited to solve for subsurface S-wave velocities. The process of estimating these velocities involves three steps: acquisition of the Rayleigh wave data, calculating dispersion curves as a function of phase velocity and frequency, and inversion of the S-wave velocity profile from the calculated dispersion curve. The components of a typical overtone image used for estimating dispersion curves are illustrated in Figure 7.

The MASW method allows for use of many channels in surface wave inversion, as opposed to the two channels used for spectral analysis of surface waves (SASW), MASW's predecessor (Stokoe and Nazarian, 1983). The biggest advantage of using multiple channels is the ability to manually interpret the dispersion curves in phase velocity-frequency space (Park *et al*, 1999). Another advantage of using multiple channels is that undesirable portions of the wavefield such as cultural noise, backscatter, and air waves can be identified and dealt with appropriately (Park *et al*, 1999).

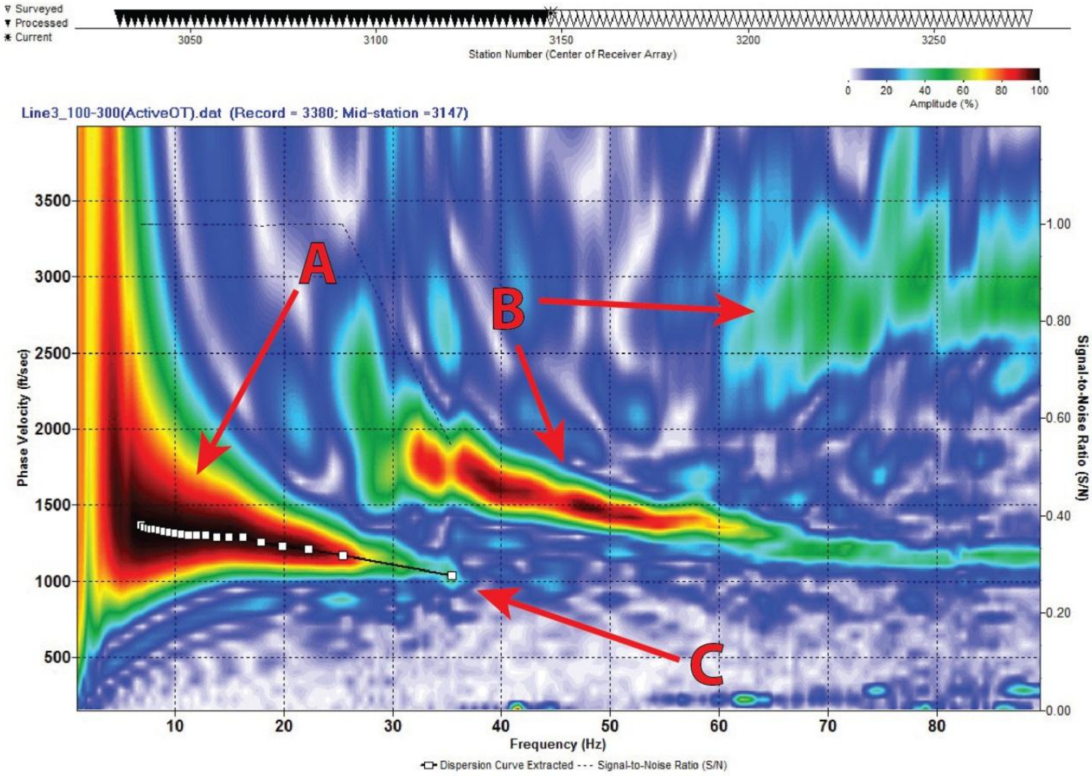

Figure 7: Figure illustrating the components of an overtone image. The overtone image represents the surface wave once it has been transformed from the offset-time domain (*x*-*t*) to the phase velocity-frequency (*v*-w) domain. A represents the energy found in the fundamental mode. B represents energy found in higher modes. C is the dispersion curve that has been picked for inversion at this location.

Since its inception, the MASW method has been identified as an extremely robust tool for providing S-wave velocity information or simply searching for anomalies in the shallow subsurface (Miller *et al.* 1999). The rest of the acquisition system is widely available due to the popularity of traditional CMP reflection surveys. In fact, the acquisition equipment and parameters are similar enough that traditional CMP reflection data can be reprocessed using the MASW method (Socco *et al*., 2009). Due to the high number of channels traditionally employed with CMP reflection methods, receivers with appropriate offsets for the MASW method can be extracted from these datasets and processed using MASW to determine S-wave velocity structure to supplement data originally acquired for P-wave reflection (Socco *et al*., 2009). However, geophones with an optimal natural frequency for a particular reflection survey may not sample the necessary lower frequencies of the surface wave to sample the desired depth of investigation.

Analysis of S-wave velocity anomalies for detecting voids in the near surface has become increasingly popular in the past 20 years (Miller *et al*., 2009, Nolan *et al*., 2011). A void has S-wave velocity of zero because it is filled with air or water, a medium with no shear strength. Considering the material encasing the void, it should be detectable as an anomalous low in the S-wave velocity field. Increased strain due to loading between sidewall supports has been shown to increase the S-wave velocity immediately above voids (Miller *et al.*, 2009; Sloan *et al.*, 2010). Together, these phenomena cause voids to appear as dipole anomalies in the S-wave velocity field.

The SurfSeis software package developed by the Kansas Geological Survey (KGS) was used to process the MASW data discussed in this study. Developed alongside the MASW method, SurfSeis was designed to make the entire processing flow user friendly. For this project, SurfSeis was used for dispersion-curve analysis, surface-wave inversion, and generation of S-wave velocity profiles. To pick data points to use in the inversion process, the data must be transformed and displayed in the frequency-phase velocity domain. Some methods available include the *f*-*k* transform (Gabriels *et al*. 1987) and slant stacking (McMechan and Yedlin, 1981). The method used in the SurfSeis software was developed by the Kansas Geological Survey (KGS) and transforms seismic data from the offset-time domain (*x*-*t*) to the phase velocity-frequency (*v*-w) domain.

Data acquisition

Data from the YPG were acquired in such a way that a large database of seismic data was available for various near-surface seismic processing methods. These data were collected primarily for general site characterization and to provide a baseline for future projects that the YPG may host. The portion of the YPG dataset used in this section was collected in a fashion similar to many shallow CMP reflection surveys. A total of 6 lines was collected with 4.5 Hz vertical geophones using a rubber-band accelerated weight drop as a source. Generally frequencies as low as one and a half octaves below a geophone's natural frequency can be used for most MASW analysis (Ivanov *et al.*, 2008). For this project only two lines were used for comparison purposes, lines 2 and 3.

There were 340 total receiver stations and 190 shot stations, three shots were recorded individually at each shot station. Seismographs used were 24 channel Geometrics Geodes with 24-bit analog-to-digital (A/D) conversion. With 24 bits of A/D conversion a wide range of particle motion can be differentiated between the noise floor of the built in amplifiers and the maximum output of these amplifiers (Steeples, 1998). The seismographs were connected with Ethernet cables which were linked with the doghouse equipment mounted in a customized John Deere Gator (Figure 8).

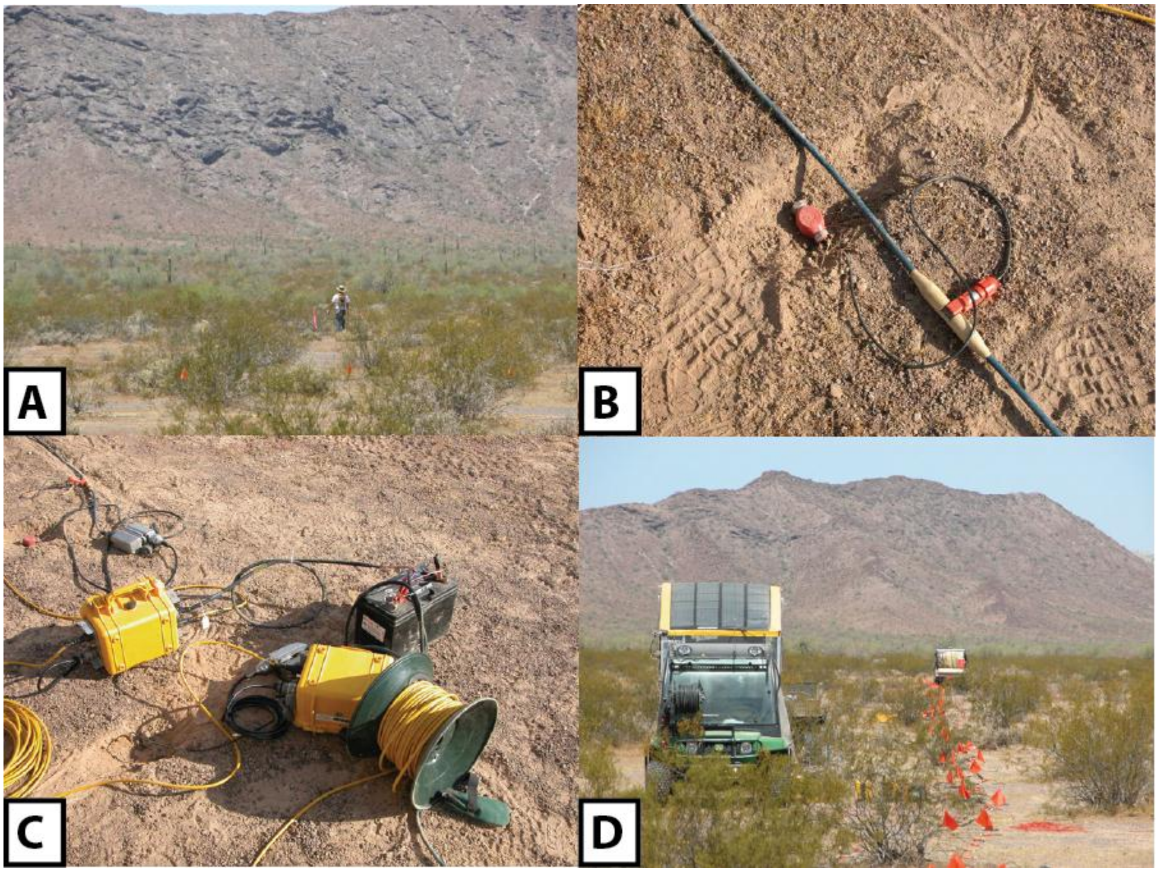

Figure 8: Photographs from the site. A.) Stations were flagged before data collection began. B.) loose surface material was removed to improve geophone coupling. C.) Seismographs were networked together. D.) Seismographs were linked to the doghouse equipment contained within the John Deere Gator. The Seismic source used was a customized Rubber Band Accelerated Weight Drop (RAWD) attached to a Bobcat Toolcat.

For MASW, the number of channels used is not as important as the maximum and minimum offset of the receiver spread (Park *et al.*, 2001). The quality of the fundamental-mode dispersion curve is influenced by where the surface wave is sampled in space. A general rule of thumb for choosing maximum and minimum offset distances is to make the spread length approximately equal to the depth of interest, and the minimum offset should be about half of that distance away from the source (Xu *et al.*, 2006). This rule of thumb is very general and should be used primarily for getting an idea of the parameters needed. Use of this rule of thumb without in-field testing may inadequately sample the surface waves (Park *et al*., 2001). Improper spatial sampling of surface waves may result in a depiction of the fundamental mode lacking higher frequencies, which will lead to erroneous dispersion curves when they are automatically picked (Ivanov *et al.*, 2008; O'Neill and Matsuoka, 2005).

Changing the maximum and minimum geophone offsets can have a variety of effects on the resulting dispersion curves. Reducing the spread length reduces the amount of horizontal averaging that is inherent to the MASW method. This would improve the lateral resolution of the final pseudo 2-D S-wave velocity profile, but may result in poor images of the fundamental mode. A larger spread generally refines the image of the fundamental mode, most noticeably in the phase-velocity domain. By using a larger spread length while maintaining the receiver station interval the fundamental mode becomes more distinguishable from higher modes (Park *et al*., 2001; O'Neill and Matsuoka, 2005).

Parameters that can vary when considering receiver offset or spread length include the minimum offset (x_1), maximum offset (x_2), receiver spacing (dx), and the number of channels (N), which is a factor of dx and total spread length (X) (Figure 9). Park *et al*. (2001) proved that increasing the number of channels increases resolution of the fundamental mode, when holding x_1 and dx constant. In a similar experiment, Park *et al.* (2001) held x_1 and x_2 constant and allowed N and dx to vary. As the number of channels decreases and dx increases, spatial aliasing occurs, which can create artifacts with low phase velocities easily mistaken for the fundamental mode.

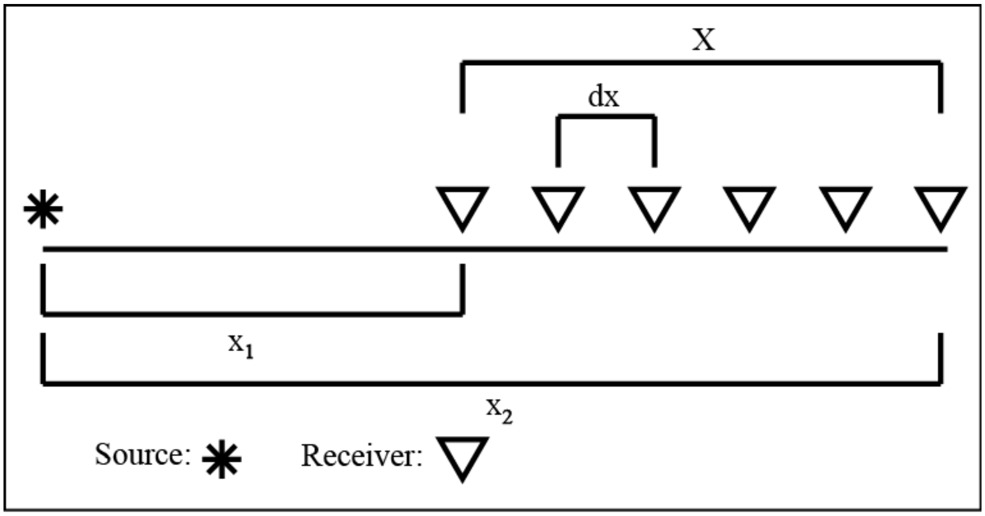

Figure 9: A schematic representing the different terms used to describe channel offsets. X1: minimum offset, x2, maximum offset, dx: receiver spacing, X: total spread length.

The testing for this project was designed to determine the most appropriate offset window for maximizing resolution of the fundamental mode while avoiding near-field and far-field effects. The method described in this section is modeled after Ivanov *et al.* (2008), by holding dx constant while N, x_1, and x_2 are allowed to vary throughout the testing process. With a fixed dx, the distance between the source and the first receiver is important parameter that must be selected to avoid introducing near-field and far-field effects. When the distance between the source and minimum receiver offset is smaller than the longest wavelength of the fundamental mode, the low frequencies in the

Rayleigh wave are not well developed; this is referred to as the near-field effect (Heisey *et. a.l*, 1982). Far-field effects include attenuation of higher frequencies, and increased energy in the higher modes (Ivanov *et al.*, 2008).

In-field testing is paramount to ensure that high-quality data is collected (Park *et al*., 2001; Ivanov *et al*., 2008). For this study, the collected data at the YPG was recorded using a traditional fixed-spread setup with more channels and offsets than necessary for a usual MASW survey. To maintain consistency from shot location to shot location, a minimum and maximum offset was selected for the optimum spread length and used throughout the processing phase to avoid creating artifacts due to spread-length changes. To choose the spread length, a wide variety of maximum and minimum offsets was tested and evaluated based on the character of the fundamental-mode dispersion curve. Criteria for evaluating fundamental-mode character included maximizing bandwidth while minimizing overlap of energy with higher modes. If the frequencies necessary for sampling the depth of interest could not be recorded, then different ranges of acquisition parameters were tested to determine if the frequencies of interest were not present.

Beginning the offset testing for the YPG dataset, Figures 10a-10h show dispersion curves generated with offset windows where the first receiver is immediately next to the source (x_1=0), x_2 ranges from 52 ft to 400 ft, and N scales with x_2. Subsequent Figures (Figures 11a-14h) are arranged with increasing x_1 but use the same spread lengths (X) to test overtone images through various combinations of x_1 and x_2. Near-field effects dominate the overtone images for spread ranges from 52 ft to 400 ft (Figures 10a-10h). Most notably, a lack of low frequencies in the fundamental mode with no useable energy below 10 Hz is evidence of near-field effects (Figure 13a).

As the spread length increases, more low frequencies are evident on the overtone images (Figure 12a-12e). The dispersion curve resulting from offset parameters using the initial rule of thumb is shown in Figure 14b. Higher-mode energy appears to be shifting the dispersion curve towards lower phase velocities. The spread geometry suggested by the rule of thumb does not resolve the fundamental mode well enough to separate it from the very energetic higher modes. Automatic picking of the fundamental mode from this overtone image would produce erroneous dispersion curve picks between 20 and 40 Hz. It is difficult to reduce the energy of the higher mode, but the resolution of each mode can be increased to minimize the interference between fundamental and higher modes (Figures 11a-11b). Each spread with an x_1 of 100 ft (Figures 12a-12h) seems to minimize the higher-mode interference best while avoiding influence of far-field effects.

The offset window chosen for picking dispersion curves for the entire dataset was 100-400 ft (Figure 10f). This offset seemed to provide reasonable fundamental mode resolution while minimizing the influence of the energetic higher mode. Dispersion curves resulting from this offset also possess higher energy levels in the 30-40 Hz range and push the useable bandwidth down to as low as 6 Hz. Based on the half-wavelength approximation, the depths of investigation for these data are between 15 and 140 ft which more than span the depth of interest for this project. According to Ivanov *et al.*, (2008) increasing the spread length and source offset distance may reduce higher-mode energy. This suggestion is consistent with these overtone images for any given x_1. However, increasing x_1 and X to very long source offsets (Figures 12h-14h) increases low-frequency higher-mode energy.

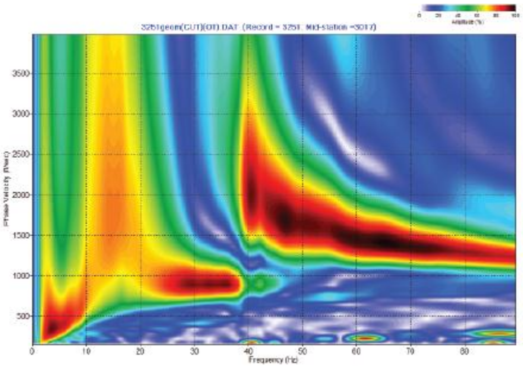

Figure 10a. Offset Window: 0-52 ft

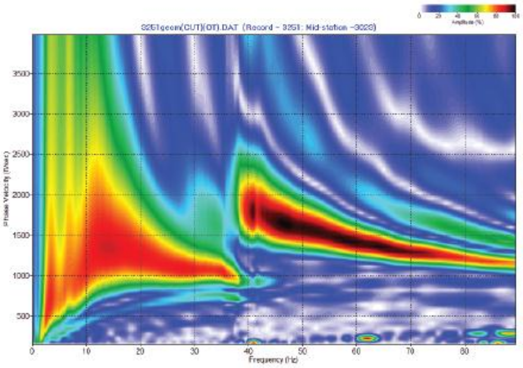

Figure 10b. Offset Window: 0-100 ft

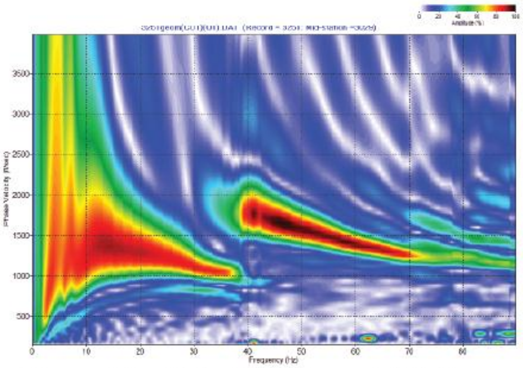

Figure 10c. Offset Window: 0-152 ft

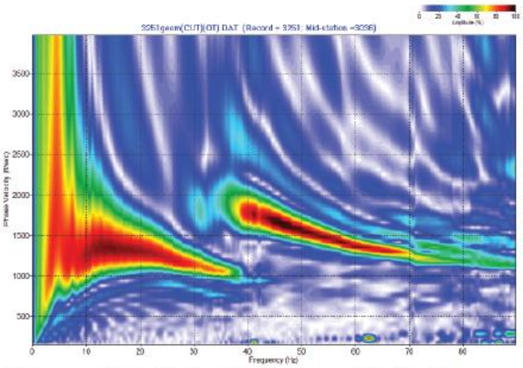

Figure 10d. Offset Window: 0-200 ft

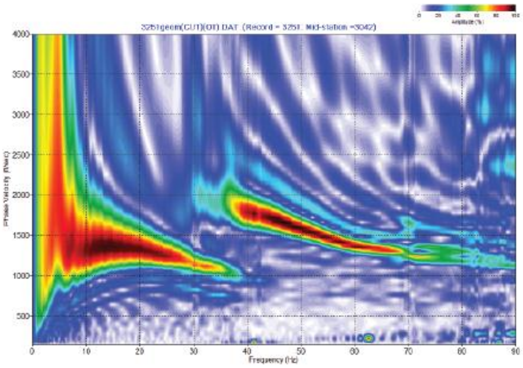

Figure 10e. Offset Window: 0-252 ft

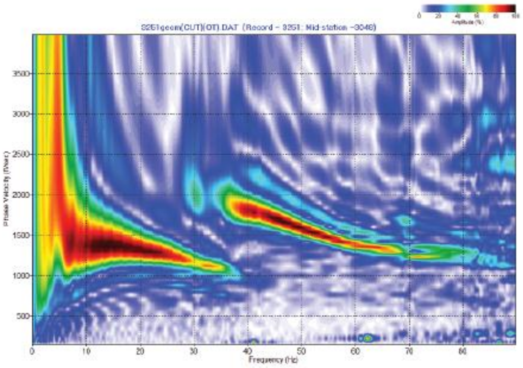

Figure 10f. Offset Window: 0-300 ft

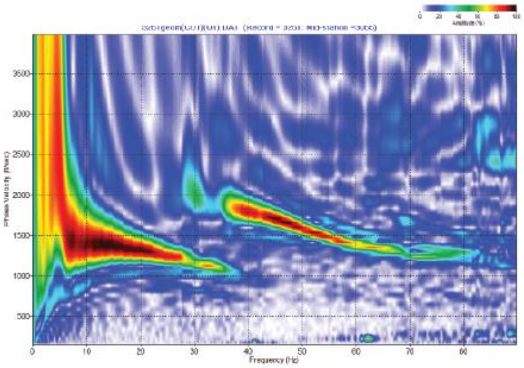

Figure 10g. Offset Window: 0-352 ft

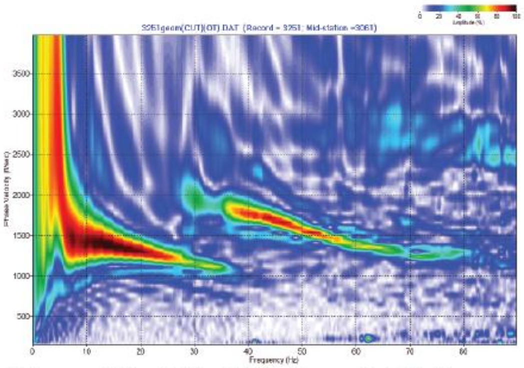

Figure 10h. Offset Window: 0-400 ft

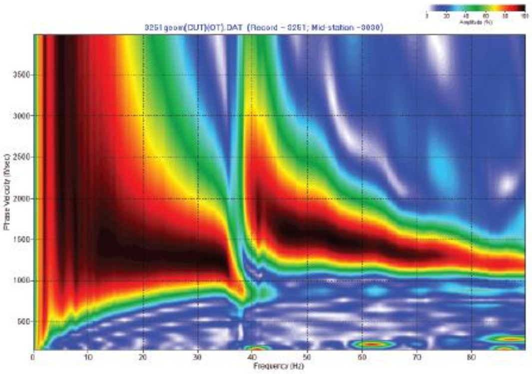

Figure 11a. Offset Window: 52-100 ft

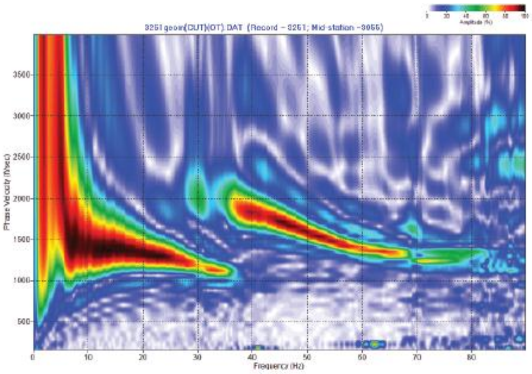

Figure 11e. Offset Window: 52-300 ft

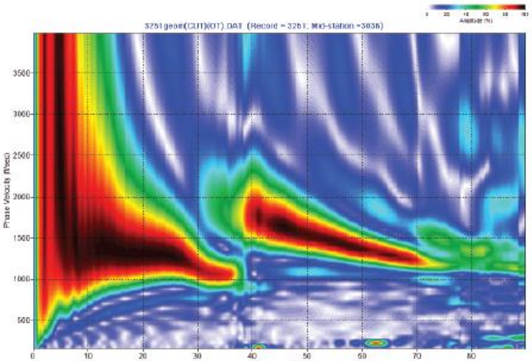

Figure 11b. Offset Window: 52-152 ft

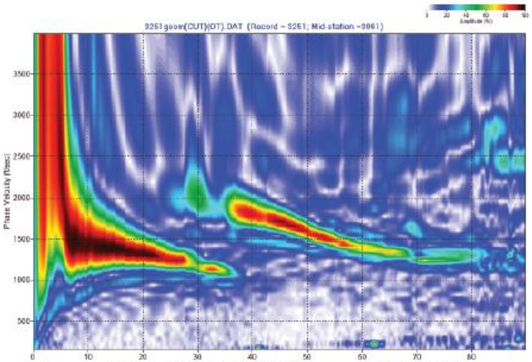

Figure 11f. Offset Window: 52-352 ft

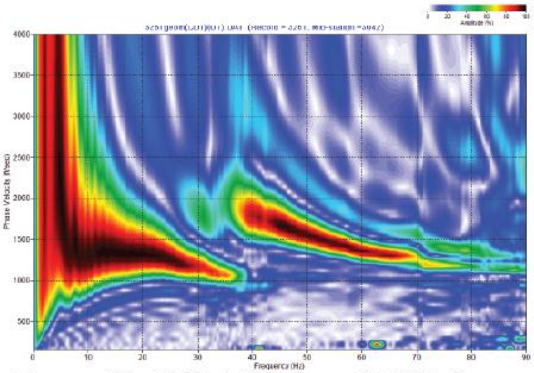

Figure 11c. Offset Window: 52-200 ft

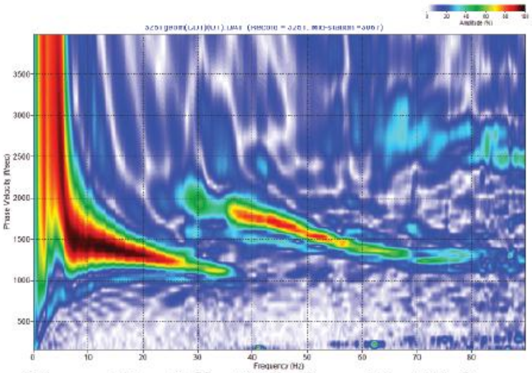

Figure 11g. Offset Window: 52-400 ft

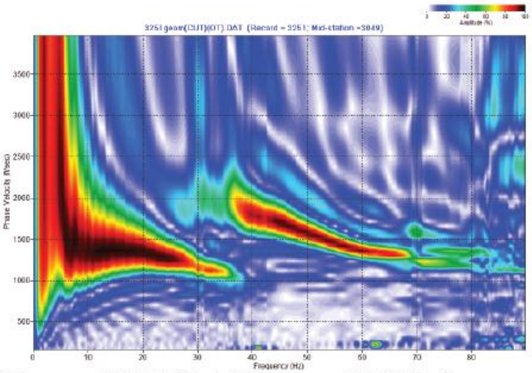

Figure 11d. Offset Window: 52-252 ft

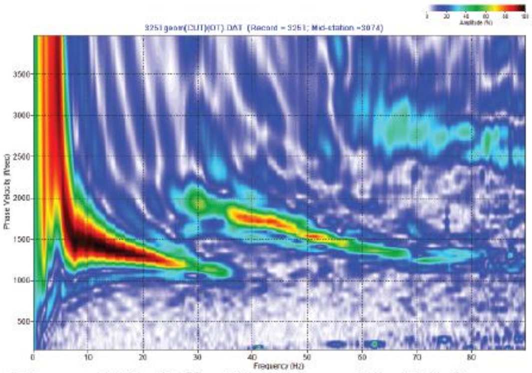

Figure 11h. Offset Window: 52-452 ft

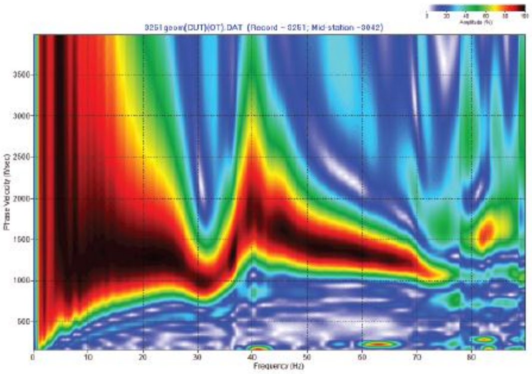

Figure 12a. Offset Window: 100-152 ft

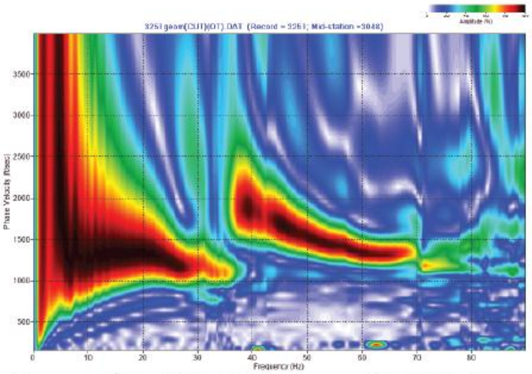

Figure 12b. Offset Window: 100-200 ft

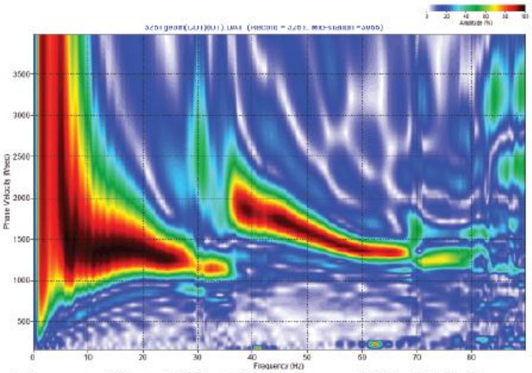

Figure 12c. Offset Window: 100-252 ft

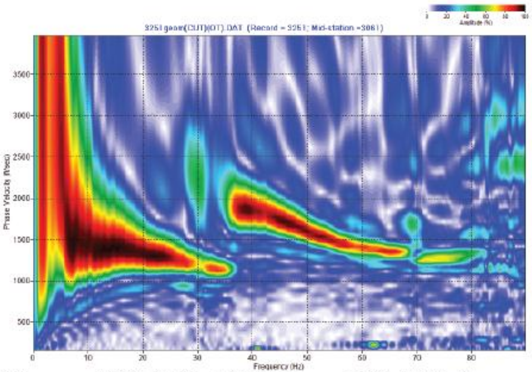

Figure 12d. Offset Window: 100-300 ft

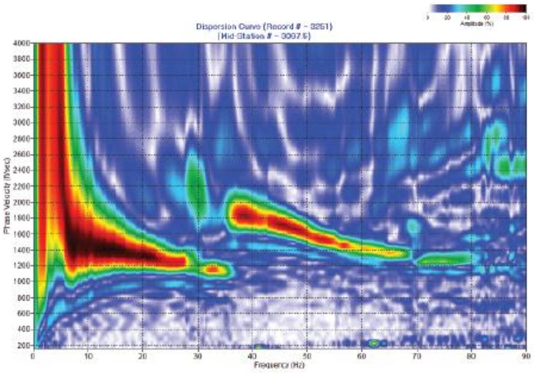

Figure 12e. Offset Window: 100-352 ft

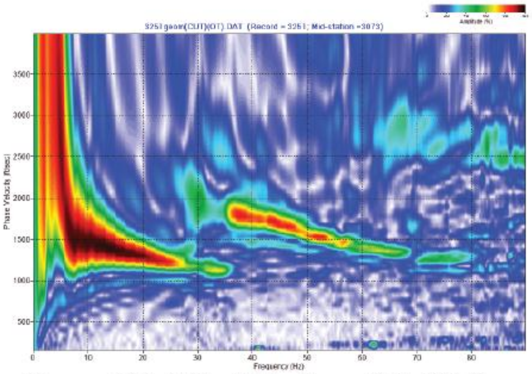

Figure 12f. Offset Window: 100-400 ft

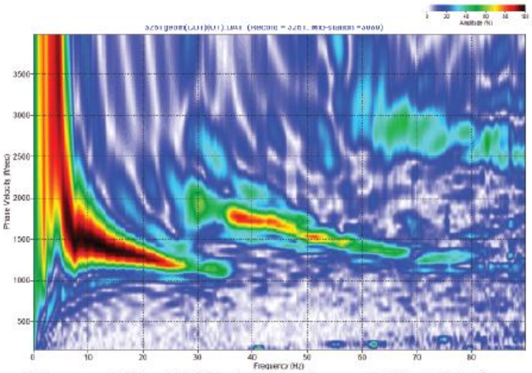

Figure 12g. Offset Window: 100-452 ft

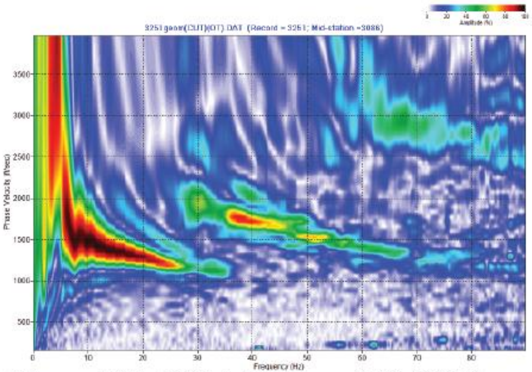

Figure 12h. Offset Window: 100-500 ft

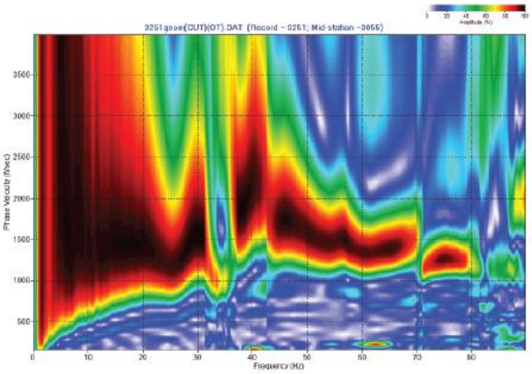

Figure 13a. Offset Window: 152-200 ft

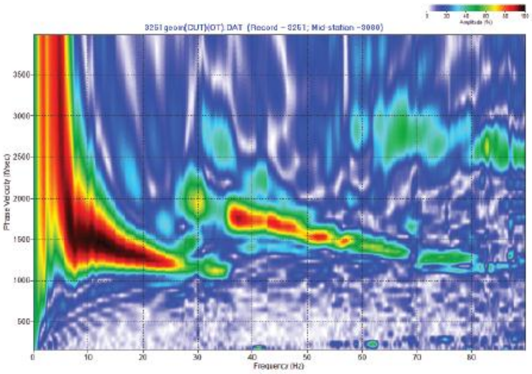

Figure 13e. Offset Window: 152-400 ft

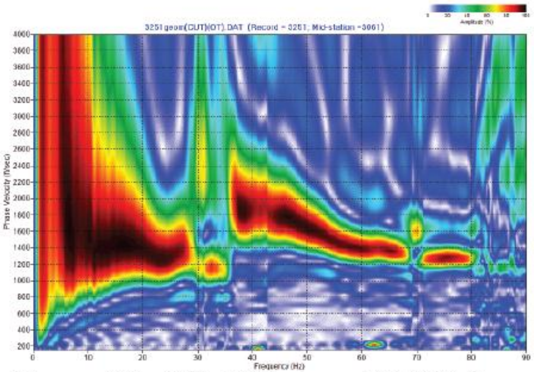

Figure 13b. Offset Window: 152-252 ft

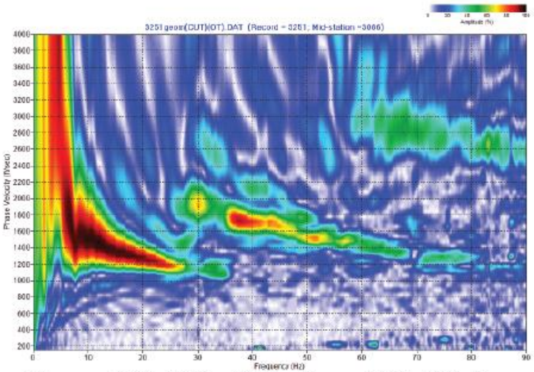

Figure 13f. Offset Window: 152-452 ft

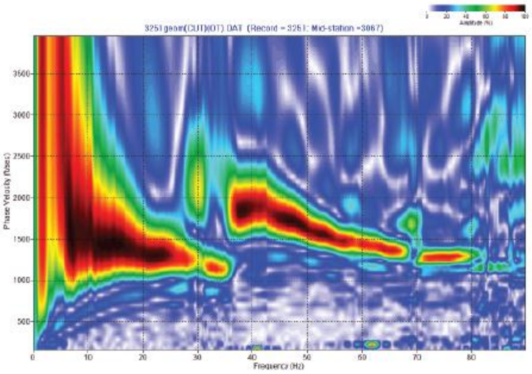

Figure 13c. Offset Window: 152-300 ft

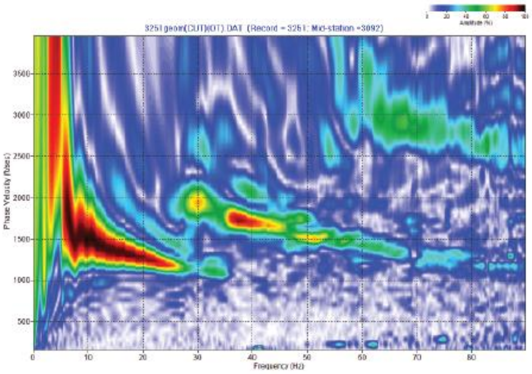

Figure 13g. Offset Window: 152-500 ft

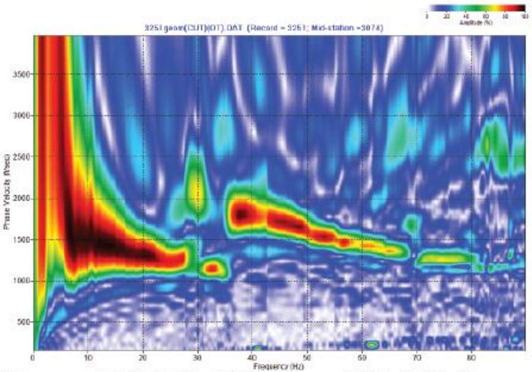

Figure 13d. Offset Window: 152-352 ft

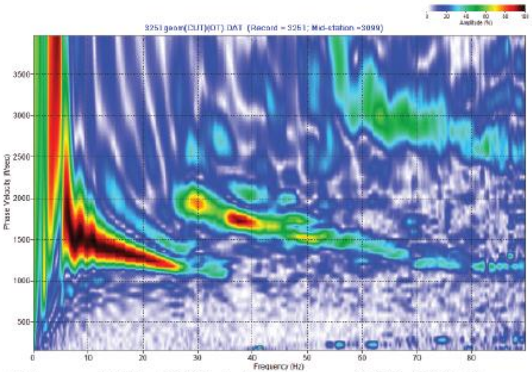

Figure 13h. Offset Window: 152-552 ft

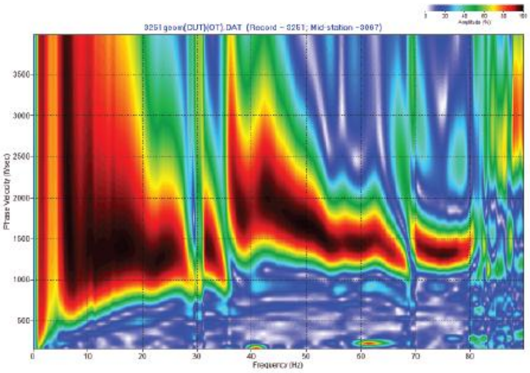

Figure 14a. Offset Window: 200-252 ft

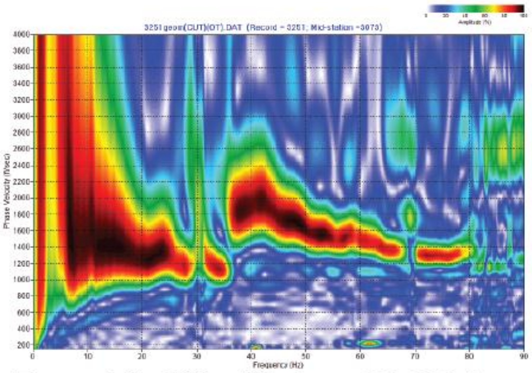

Figure 14b. Offset Window: 200-300 ft

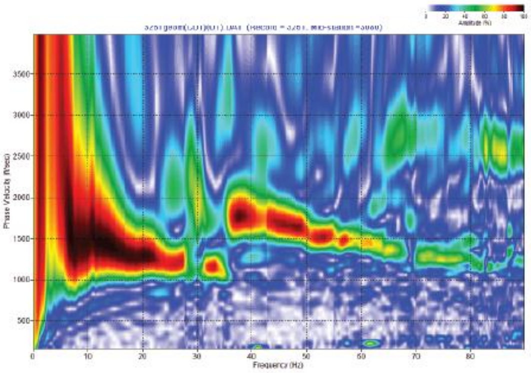

Figure 14c. Offset Window: 200-352 ft

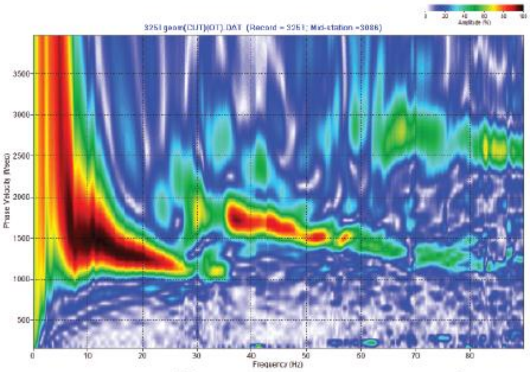

Figure 14d. Offset Window: 200-400 ft

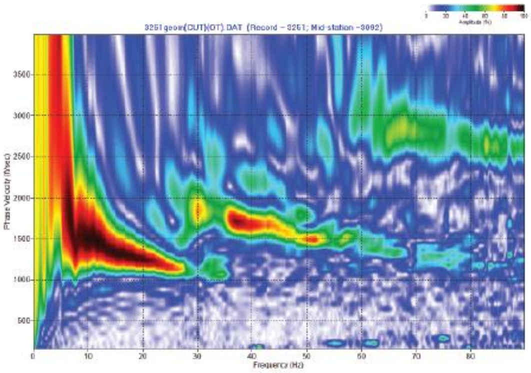

Figure 14e. Offset Window: 200-452 ft

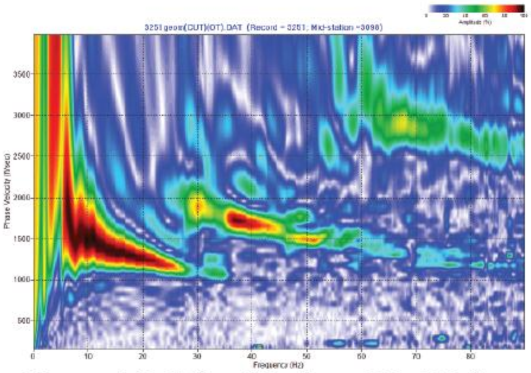

Figure 14f. Offset Window: 200-500 ft

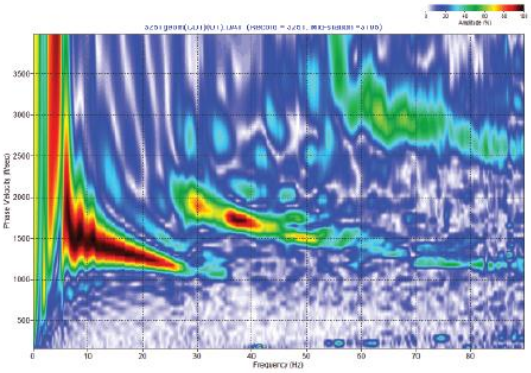

Figure 14g. Offset Window: 200-552 ft

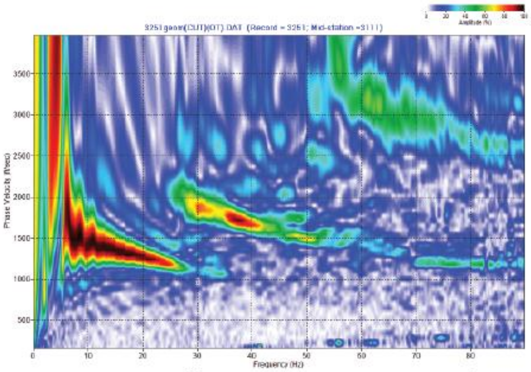

Figure 14h. Offset Window: 200-600 ft

Dispersion Curve Picking

Parameters used for automatic dispersion curve picking must be adjusted appropriately to ensure that each curve is picked accurately. The two selectable parameters in this phase of processing are the number of points automatically picked, and the percentage of curve smoothing applied to the automatic curve picking. SurfSeis will pick points on the dispersion curve by identifying points with the highest amplitude within the bounded areas selected by the user. Selection of the proper bounding areas is extremely important to help separate the fundamental mode from the energetic higher modes in the case of the YPG dataset. Because the software only targets amplitude maxima, boundaries isolating the fundamental mode keep the program from automatically picking higher modes.

The automatic dispersion curve picking parameters used for the YPG dataset constrained the software to 20 points with 5% curve smoothing. Increasing the smoothing constraint to 15 % makes the automatically picked dispersion curve linear, deviating from the interpreted trend of the fundamental mode. Automatic picking with no smoothing is preferable in cases where the fundamental mode is energetic and noise free, but smoothing can be useful in some cases where fundamental mode is obscured by noise or higher-mode energy

Using the source offset range of 100 to 400 ft the fundamental mode can be picked with confidence between 6 and 35 Hz on every overtone image, and up to 45 Hz and even 55 Hz in many locations. The fundamental mode is dominated by energetic higher modes at these higher frequencies. The amplitude of higher-mode energy fluctuates between 20 and 30 Hz at different locations, leaving the fundamental mode with a much larger signal (Figure 15) while partially obscuring the fundamental mode in others (Figure 16). The higher mode almost completely obscures the fundamental mode from 30 to 60 Hz, making the inversion results of the upper 20 ft much less reliable. In other instances the higher mode has less energy in a specific frequency range, giving it a “spotty” character on the overtone images (Figure 17). These breaks in higher mode energy provide confidence in interpreting dispersion curves on data where the fundamental mode is less energetic. Most of the dispersion curve points were picked where the fundamental mode represented less than 50% of the amplitude observed on overtone images in the lower frequency portion.

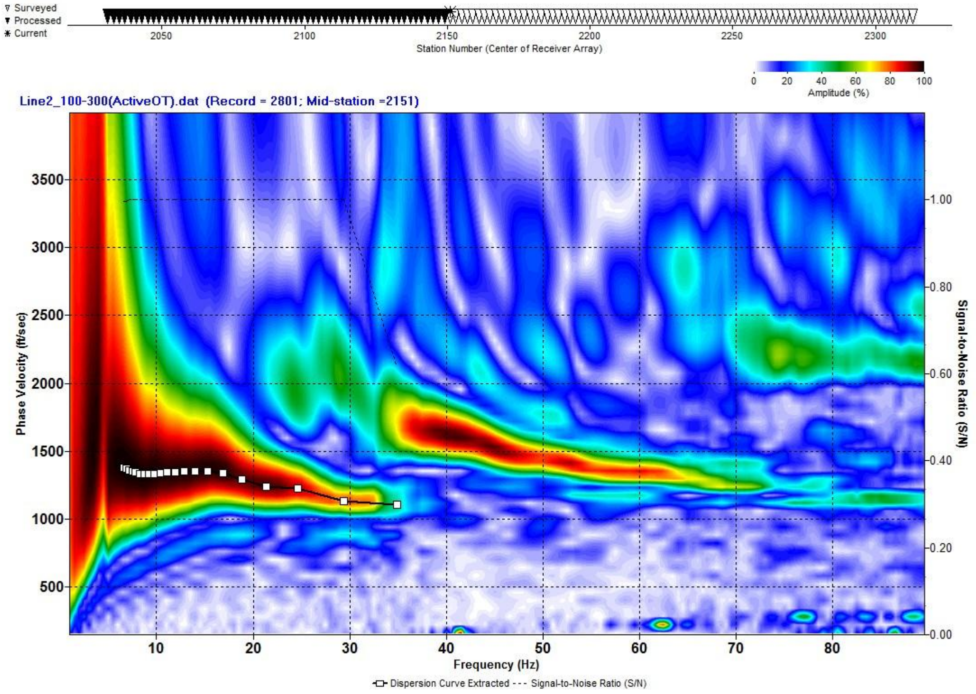

Figure 15. Overtone image displaying relatively high energy in the fundamental mode out to 33 Hz.

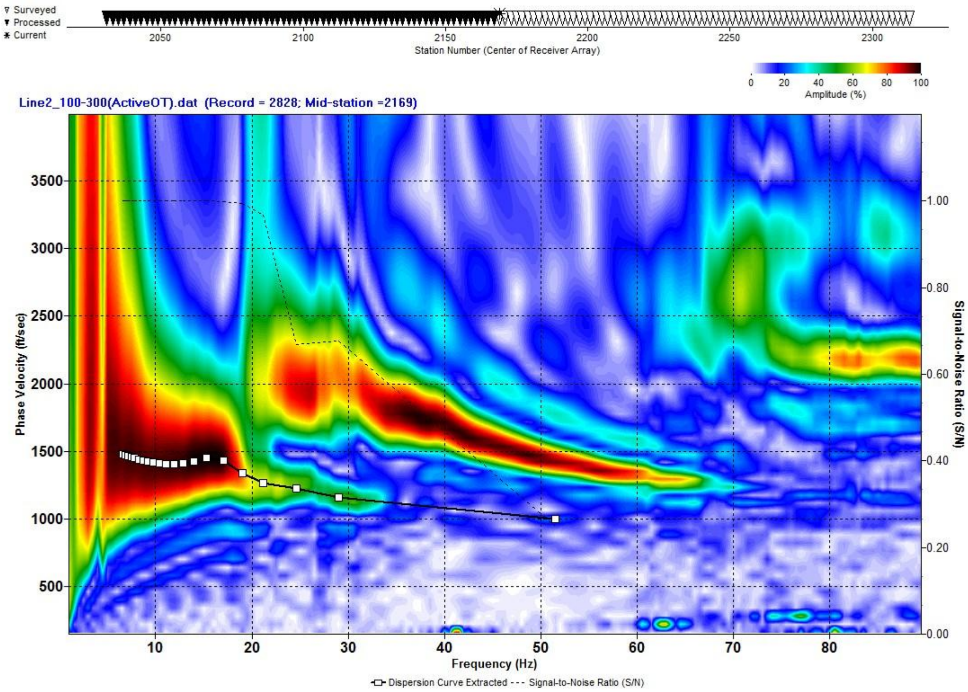

Figure 16. Overtone image with relatively high energy in the higher mode, reducing confidence of fundamental mode picks above 20 Hz. Notice that the difference between the fundamental mode dispersion curve picks shows very little difference from Figure 15.

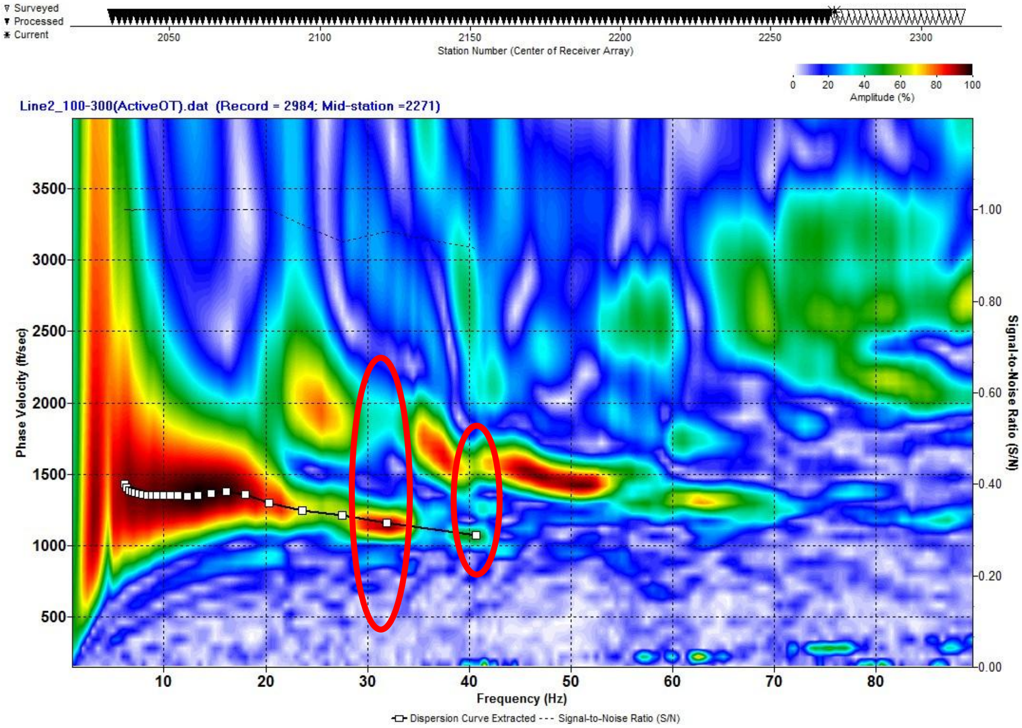

Figure 17. This overtone image is an example where certain frequency components of the higher mode have less energy than the fundamental mode, allowing glimpses of the fundamental mode as is depicted in the red circles. These overtone images are rare throughout both lines, but can be used to verify the position of the fundamental mode when picks are made on overtone images with lower signal-to-noise ratios.

Inversion

Dispersion curves interpreted from the overtone images were inverted using an initial model with ten layers. The layer thicknesses in the model gradually increased from 3 ft to 18 ft on a logarithmic scale. Ten layers with increasing thicknesses are the default initial model for SurfSeis, based on the assumption that ten layers is more than enough to accurately discretize the subsurface (Xia *et al.*, 1999). The root-mean-square (RMS) error between the measured data points and modeled dispersion curve points generally converged to within 1% of each other after 10 iterations. The initial velocity model for each location was calculated based on the range of frequencies present in the sampled surface wave. According to Ewing *et al.* (1957), Rayleigh wave phase velocities relate to S-wave velocities by approximately:

$$c_R \cong 0.9V_s \quad \textbf{(6)}$$

where c_R is phase velocity and V_s is S-wave velocity. This relationship was used to estimate the initial S-wave velocity for each layer. Assuming that a Rayleigh wave travelling at a specific phase velocity penetrates about one half of a wavelength, these phase velocities can be used to estimate S-wave velocities for each layer in the initial model.

Results

Once the inversion process is completed, the resulting velocity profiles are combined to produce the pseudo 2-D velocity profiles displayed in Figure 18. Laterally the S-wave velocity changes very little, but clearly there is a low-velocity layer appearing at around 50 ft deep. Xia *et al*., (2005) demonstrated that the MASW method can image low-velocity layers with variation down to 2% when compared with S-wave velocities from borehole data. The low-velocity layer in that case was about 25% lower than the velocity of the overlying layer, and was contingent on extreme accuracy of dispersion curve picks.

Verification of the low-velocity layer is possible with downhole seismic-velocity analysis. There appears to be a depression on line 3 between station 3175 and 3215 (Figure 18). This may be an ancient channel filled with the material that the high-velocity layer is composed of. This interpretation is reasonable because the depositional environment within the Yuma basin has been documented as an alluvial terrace (Eberly and Stanley, 1978; McDonald, 2009). The dispersion curves support the presence of this channel with higher phase velocities than the rest of the line around 10 Hz, corresponding to the higher S-wave velocities around 70 ft in the vicinity of the channel.

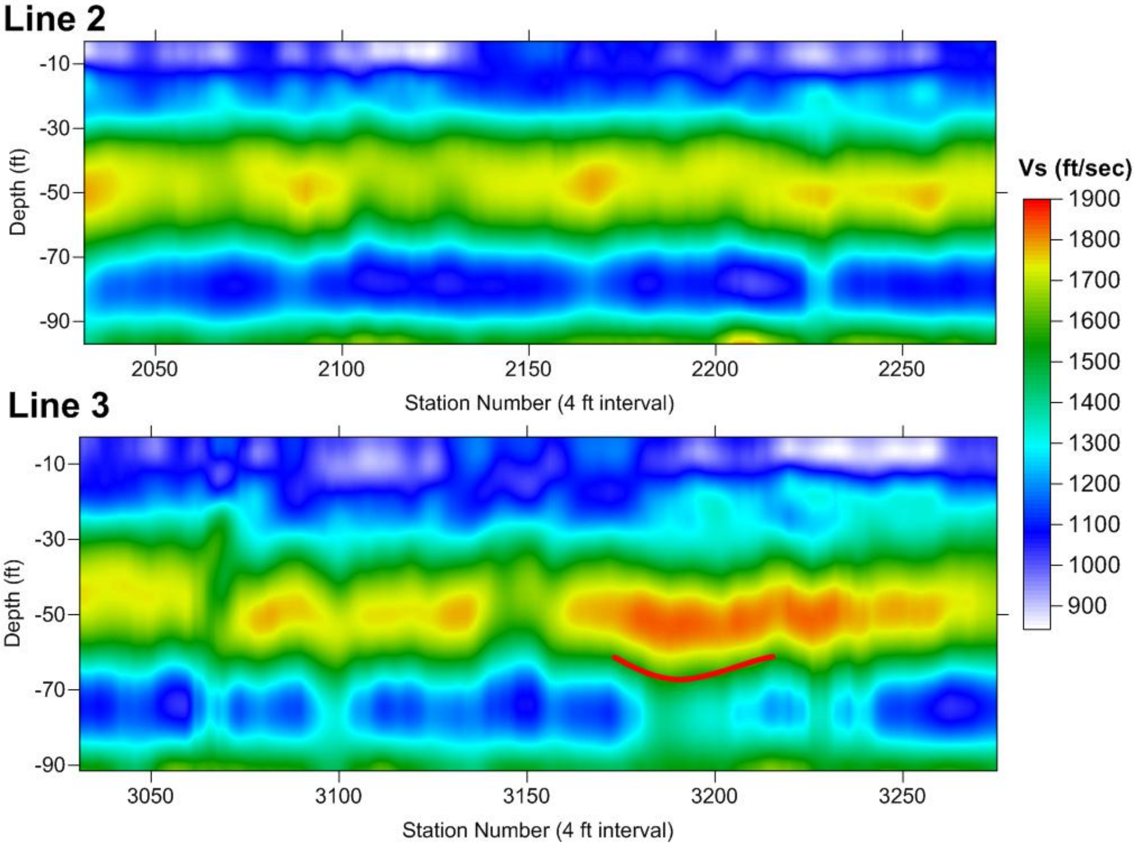

Figure 18: Pseudo 2-D S-wave velocity profile resulting from MASW inversion. Notable features include a high-velocity layer overlaying a low-velocity layer. There appears to be an incision into the low-velocity layer indicated by the red line (line 3).

Vertical resolution in the MASW method has been proven to be directly related to how well-defined the fundamental mode is on the overtone image in the phase-velocity domain (Xia *et al.*, 2005). If the image of the fundamental mode were infinitely thin in the phase-velocity domain on the overtone image, the dispersion curve points would be infinitely accurate to the true model, and the inversion algorithm would recover the true S-wave velocities with 100% accuracy (Xia *et al.*, 2005). This implies that the vertical error, or vertical resolution of a dataset is directly related to the range of phase velocities within the high amplitude portion of the overtone image along a given frequency. Vertical resolution during the inversion process is determined by the thickness of each layer, while horizontal resolution can be as high as 1/6th of the spread length (Ivanov *et al.*, 2006c). In this case, the thicknesses of the 10 layers ranged from 3 to 17 feet, and 1/6th of the spread gives a horizontal resolution of 50 ft.

S-wave Tomography

Introduction

The basic idea of tomography was established in the early 1900's when Johann Radon showed that the inside of an object can be imaged if projections through the object can be measured (Stewart, 1991). The practice of tomography has become well established in modern medical imaging. The success of medical tomographic methods has made CAT scans (Computed Axial Tomography) and MRIs (Magnetic Resonance Imaging) household names (Stewart, 1991). Tomography has found much success in geophysics as well, though the method is more challenging geometrically (Kanli, 2008). In fact, it has become common practice to run geological core samples through CAT scans to help determine composition and image bedforms for oil exploration (Stewart, 1991).

Medical tomography has advantages over seismic tomography through smaller scale, limited range of media, and fully-encompassing receiver geometry. Medical tomography generates images on the scale of millimeters, while the scale for seismic tomography generally ranges from meters to tens of kilometers. X-rays are assumed to be non-dispersive, while that assumption cannot be made with seismic waves (Stewart, 1991). The frequencies analyzed in these methods are affected by scale as well, where the short ray paths in medical tomography allow much higher frequencies than are typically sampled with seismic tomography (Kanli, 2008). The largest advantage that medical tomography has over seismic tomography is acquisition geometry. In medical tomography, sources and receivers are in place in a complete circle around a sample, sampling ray paths from 360 degrees around the object to be imaged (Kanli, 2008).

In geophysics, an optimized geometry would involve sources and receivers in two boreholes and on the surface. Typical seismic tomography confines sources and receivers to the surface, which presents significant challenges for the method such as insufficient ray coverage and multiple arrival paths (Kanli, 2008, Crice, 2011). By restricting sources and receivers to the surface, the method is forced to rely on diving ray paths that originate from the surface and return to the receivers on the surface. Diving-ray tomography relies on the assumption that velocity increases with depth, and has the best ray coverage when using an initial model with linear velocity functions rather than homogenous layers (Kanli, 2009).

Seismic diving-wave tomography has great difficulty imaging hidden layers and low-velocity layers. The hidden-layer phenomenon occurs when the velocity of one layer of rock is lower than the velocity of layer below it with a much higher velocity, enabling refractions from the higher-velocity layer to arrive before refractions from the lower-velocity layer (Ivanov *et al.*, 2006b). Velocity inversions cannot be imaged for a similar reason, seismic energy preferentially propagates through faster layers, reducing ray coverage in areas with relatively low velocities. On a seismogram the first arrivals from the faster layer above the low-velocity layer will always arrive sooner than signal from the slower layer (Kanli, 2008).

To image the media that the seismic waves are propagating through with tomography, ray paths must be modeled in space to associate with their respective measured travel times. To do this, Vidale's expanding-time-field method (Vidale, 1988) is used to calculate the travel time from the cells directly adjacent to the source, to the cells directly surrounding them. By applying Hyugen's principle, these adjacent cells are treated as new point sources and travel times for each cell are calculated as the wavefront propagates through the velocity model. This is the forward modeling step (Kanli, 2008). To determine the ray paths of the first arrivals for the inversion process, the ray paths with the minimum travel times must be selected. This is accomplished by following the steepest gradient in travel time from the receiver back to the source (Kanli, 2008). Once the ray paths are calculated, the velocity for each cell through which a ray has passed is slightly modified in an attempt to bring the calculated travel times closer to those observed. There are a number of different methods for correcting these velocities. Examples include the simplest form, back projection, and the more accurate simultaneous iterative reconstruction method or SIRT (Stewart, 1991; Kanli, 2008).

Data Acquisition and Interpretation

The S-wave refraction tomography data were acquired with parameters similar to the data used for MASW. The source was a 16 lb sledgehammer striking a shear block (Figure 19). 14 Hz Geospace horizontal geophones were used in conjunction with the Geometrics Geode seismograph system described in the previous section. Both the geophones and the shear block were oriented perpendicular to the lines. 240 channels recorded energy from receivers spaced at 4 ft intervals. The source interval was 96 ft which provided sufficient ray coverage to reduce nonuniquness during the inversion process. To identify the first arrivals for each trace, shots with the same source orientation and location were stacked and a filtered with a high cut filter beginning at 55 Hz. The filter rolloff extended to 100 Hz to minimize altering the phase of the first arrivals. This provided high-quality first-arrival events as far as 500 ft from the source.

The first-arrival times were picked using KGS SeisUtilities and exported to a file format useable by the KGS software TomSeis. All data used in this section comes from line 3, results for line 2 are similar to line 3 and therefore prove no additional information.

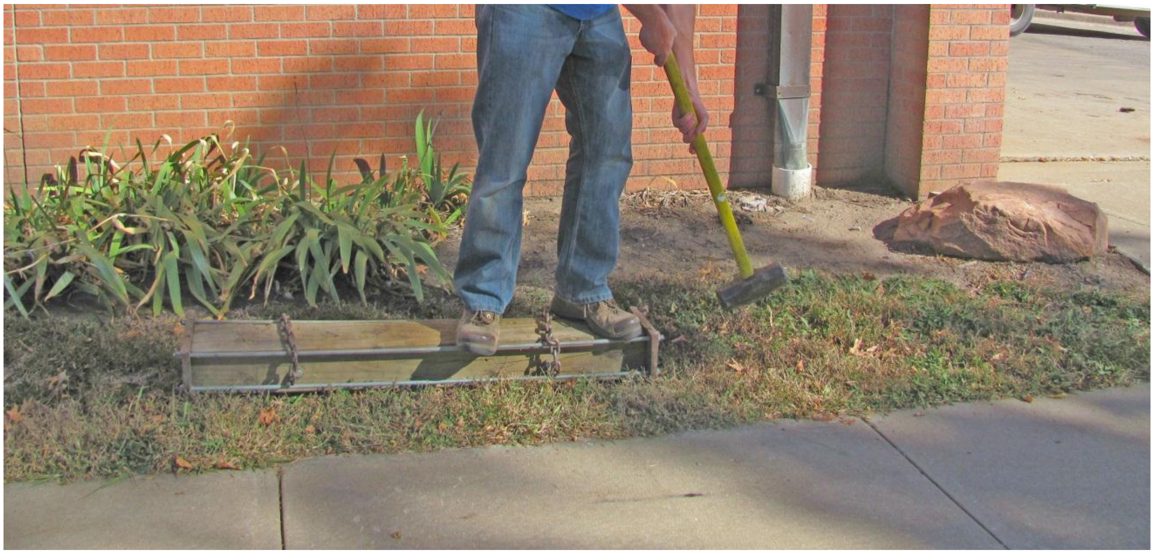

Figure 19: Picture of a shear block used to generate S-waves. The device consists of a block of wood capped with steel plates with teeth for gripping the earth on both ends. Either end of the block is struck to generate S-waves. The person swinging the hammer stands on the block to improve coupling and reduce the risk of inelastic deformation.

Initial Velocity Model Selection

Conventional refraction analysis is based on abrupt velocity discontinuities. The refraction model assumes the near surface is discretized into homogenous layers where the velocity increases suddenly at layer boundaries. First arrivals, in this case, would arrive along linear trends. Diving-ray tomography provides raypath modeling for cases where first arrivals are not perfectly linear, which is often the case. For diving-ray tomography to work, velocities must increase monotonically with depth (Kanli, 2009).

Though the true shallow velocity structure is likely to be a combination of both discretized and linear velocity gradients, assumptions must be made based on local geologic information to select an initial velocity model that will lead to the true solution. For example, an area consisting entirely of unconsolidated sediment should have velocities that increase linearly with depth due to compaction. However, a two-layer refraction model may better represent abrupt velocity changes between two layers, for example where caliche layers have developed in otherwise unconsolidated sediments (Ivanov *et al*., 2006b; Kanli, 2009). The true solution may be a combination of these two models, which is considered in this study as well.

Refraction velocity model

One method for determining an appropriate initial model is conventional refraction analysis (Kanli, 2009). This approach provides a good approximation when observed first arrivals appear to be composed of distinct linear segments (Figure 20). The linearity of the first arrivals observed in these data suggests that refraction analysis may provide a reasonable initial velocity model. The refraction-based initial model in this study consists of two layers consistent with the two distinct linear first-arrival patterns observed on shot gathers. The velocities for the first and second layers were calculated where V_0 = 800 ft/sec and V_1 = 1700 ft/sec. The depth of the first layer (z) was calculated by:

$$\boldsymbol{z = \frac{X_C}{2}\sqrt{\frac{V_1 - V_0}{V_1 + V_0}}} \qquad \textbf{(7)}$$

where X_C is the crossover distance, which is 28 ft (Figure 20). These values yield a thickness of 2 ft for the first layer. Beyond 28 ft, the first arrivals follow a consistent velocity trend approximately 1700 ft/sec (Figure 21). Based on a range of seismograms, an initial model was generated with an 8 ft deep layer with a velocity of 800 ft/sec, a halfspace with a velocity of 1700 ft/sec, and 8 ft by 8 ft cell size.

Manual adjustments optimized the initial model, so the inversion reached a solution in as few iterations as possible. The refraction-based initial model in this study was created by comparing observed and calculated travel times after the first forward model, modifying the model slightly, and repeating the process until the calculated first arrivals reasonably matched (Figure 22) (Ivanov *et al.*, 2006b). This model is homogenous with a velocity of 1700 ft/sec below the 8 ft thick surface layer of material with a velocity of 800 ft/sec. Upon completion of the first forward model, the RMS error between observed and calculated first arrivals is less than 6 ms, meaning that the model was initially close to being a reasonable solution for the tomographic inversion. However, it is geologically unreasonable that unconsolidated sediments at this site would be so homogenous, especially when the grain size can vary significantly within a few feet (Reading, 1996). After the initial inversion step, the step function is smoothed into a velocity gradient, increasing the RMS error by a factor of five. Through successive iterations the velocity model converges on the final solution (Figure 23).

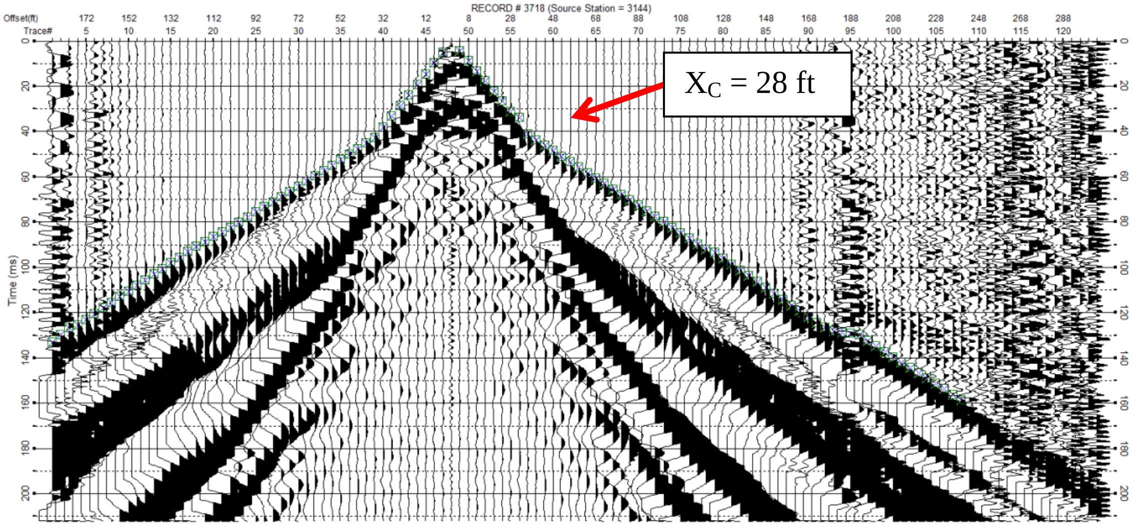

Figure 20: S-wave data collected along line 3. A 60 Hz high-cut was filter applied to image first arrivals at far offsets. First-arrival picks represented by green boxes.

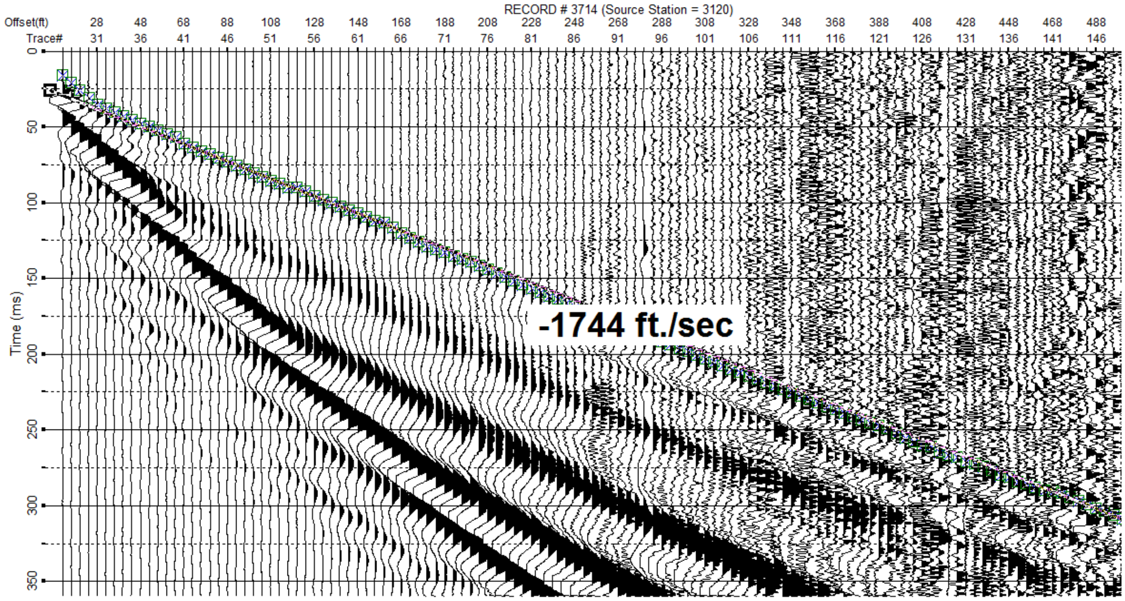

Figure 21: First arrivals displayed on the raw data from line 3. The linear pattern of first arrivals is consistent throughout lines 2 and 3. The longer offsets were picked with the aid of a high cut filter. This linear trend suggests use of the refraction model is appropriate.

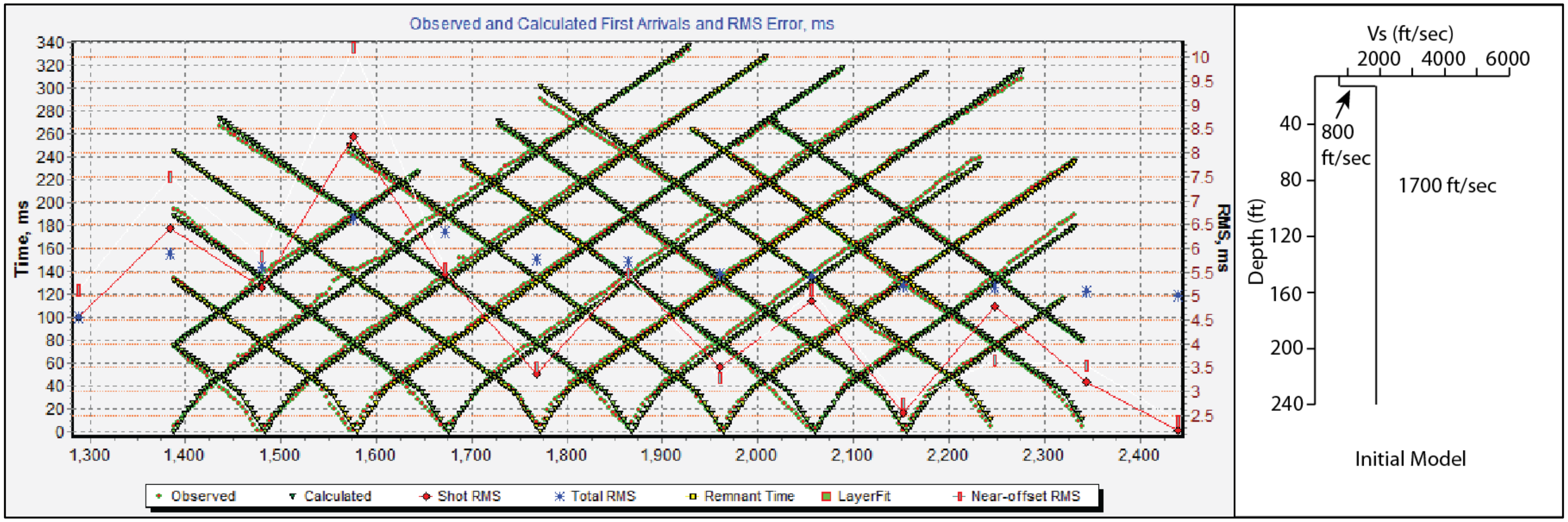

Figure 22: Initial model based on refraction analysis and the resulting calculated arrival times from the first forward model. Prior to the first inversion, the RMS error was less than 6 ms, suggesting this initial model is extremely close to an actual solution.

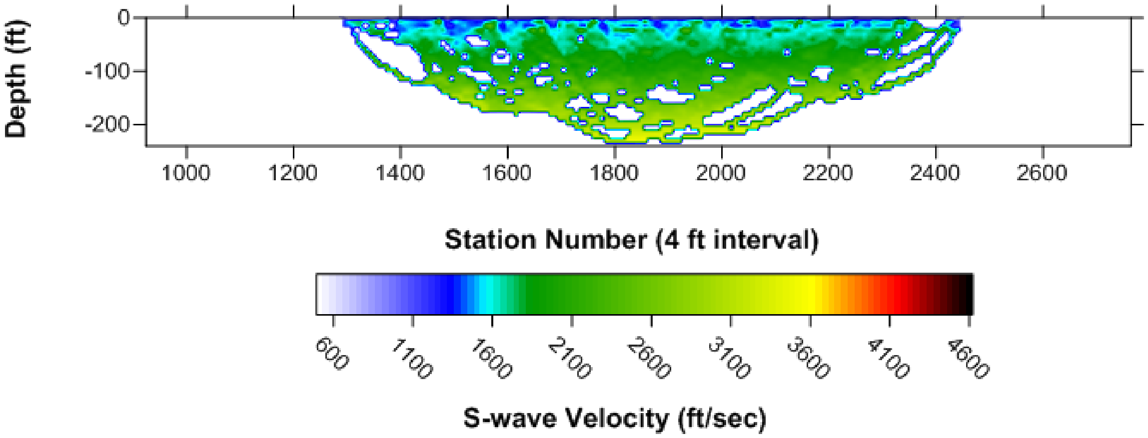

Figure 23: Final solution to the refraction-based initial model. The step velocity function is completely smoothed over, even after adjusting the parameters in an attempt to preserve a step-like velocity function throughout the inversion process.

Linear velocity model

Knowing the shallow material in the study area site consists of unconsolidated alluvial sediments above the water table (Miller *et al*., 2010), the initial assumptions were that seismic velocity would increase linearly with depth (Kanli, 2009). The shallowest velocity in the linear velocity function begins at 1300 ft/sec and increases linearly to 5300 ft/sec at the deepest layer. The initial RMS error from the first forward model is 14 ms, larger than the first forward model of the refraction-based initial velocity model. The observed and calculated first-arrival trends are different (Figure 24). However, the inversion process converges on a solution within 10 iterations with a total RMS error of 4 ms. The solution is strikingly similar to the solution from the refraction-based initial model, but with somewhat lower velocities (Figure 25).

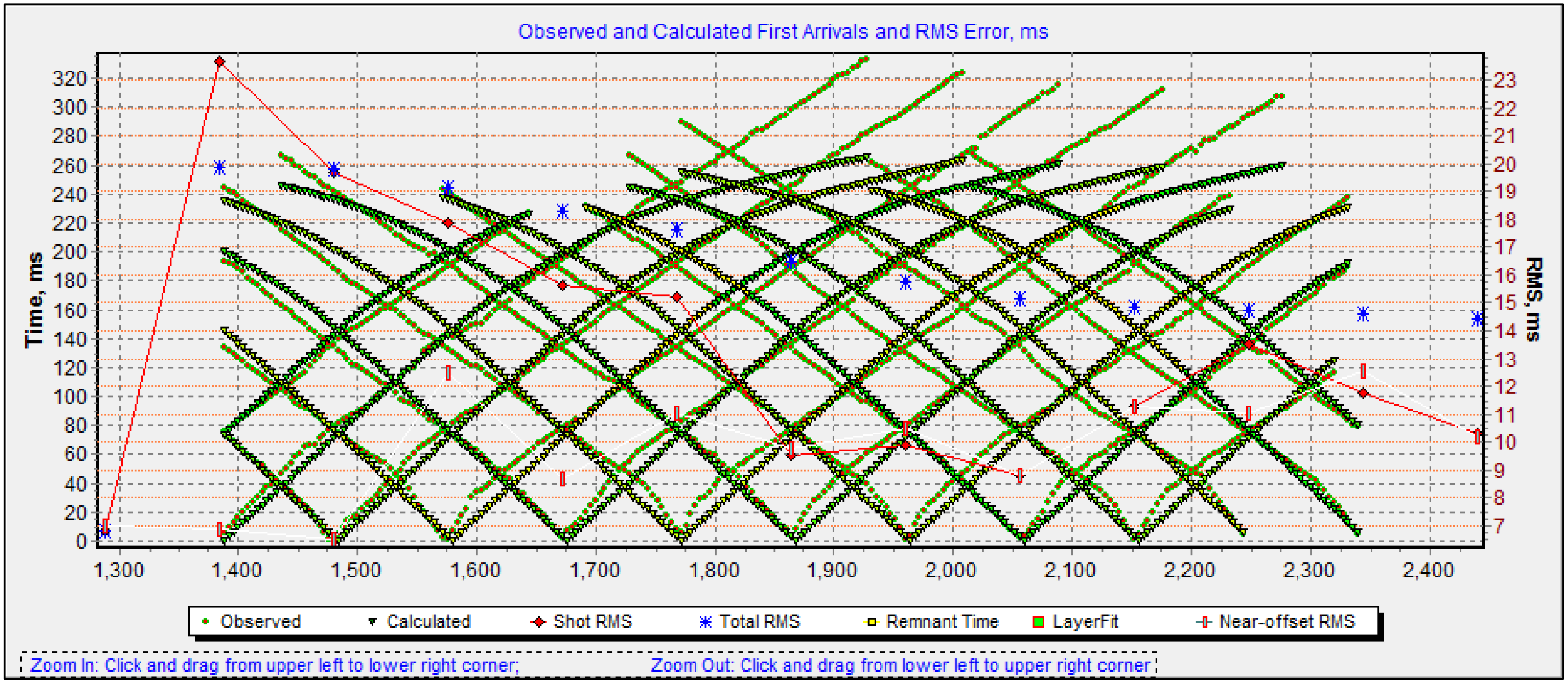

Figure 24: This figure illustrates the difference between calculated and observed first arrivals from the linear velocity function initial model.

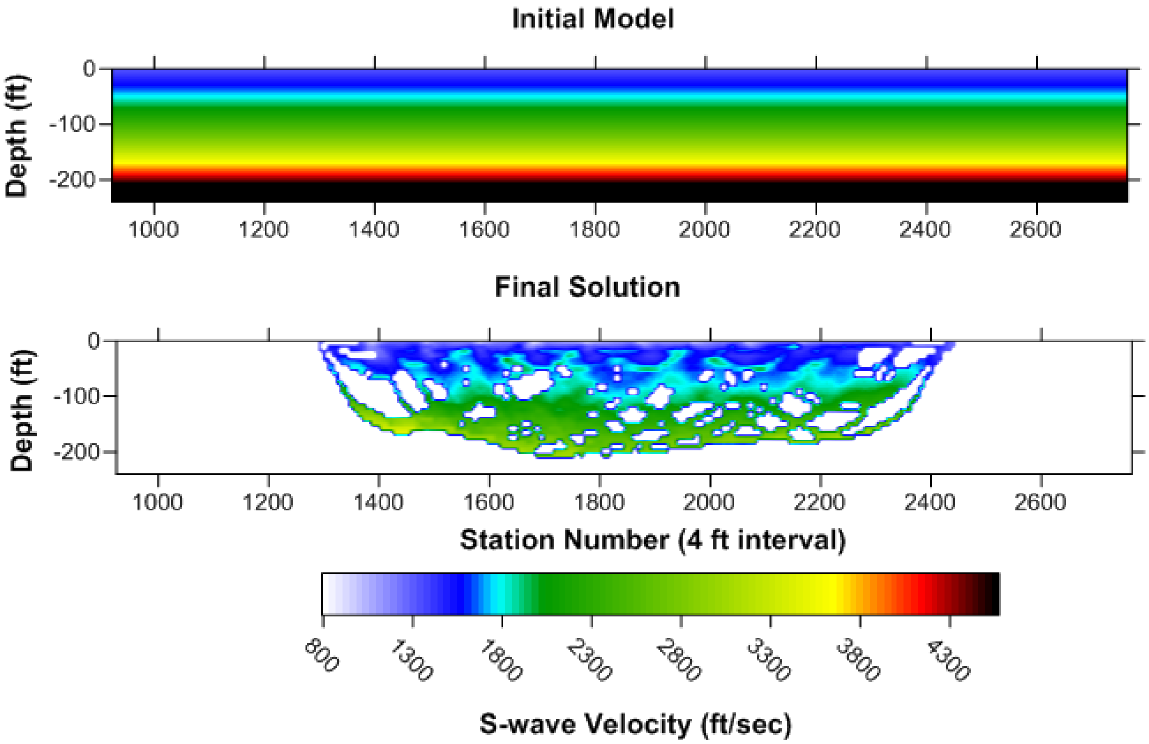

Figure 25: The initial linear velocity model and corresponding solution. The solution converged within 10 iterations and has a final RMS error less than 4 ms.

Model based on MASW

Having applied two traditional methods of developing initial velocity models, the next step is to use a model based on the MASW results discussed previously. Stabilizing devices (damping and smoothing effects) provide only qualitative *a priori* information, and the two previous models are based only on geologic assumptions. Using MASW results integrates geologic data derived from the site (Ivanov *et al.*, 2006b). The top 12 rows of cells in the model were based on the MASW results, while the deeper portion was increased linearly to 3000 ft/sec.

There was a striking similarity between the calculated and the observed arrival-time trends (Figure 26). This model was not subjected to the same preconditioning as the previous models, and there were no adjustments based on forward models. Within the first iteration the model seems to fit very well, though the initial RMS error is 23 ms. The crossover distance is larger for the first arrivals from the MASW-based model, suggesting that the MASW results place the 1700 ft/sec layer deeper than the refraction analysis. This occurs due to the higher mode obscuring the higher frequency portion of the fundamental mode. The layer below the 1700 ft/sec layer is not represented in these arrival times because the back-projected ray paths do not penetrate the lower velocity layer, even though the velocity gradient is gentle and based on real data (Figure 27). Once the inversion is completed, the low-velocity layer is removed (Figure 28).

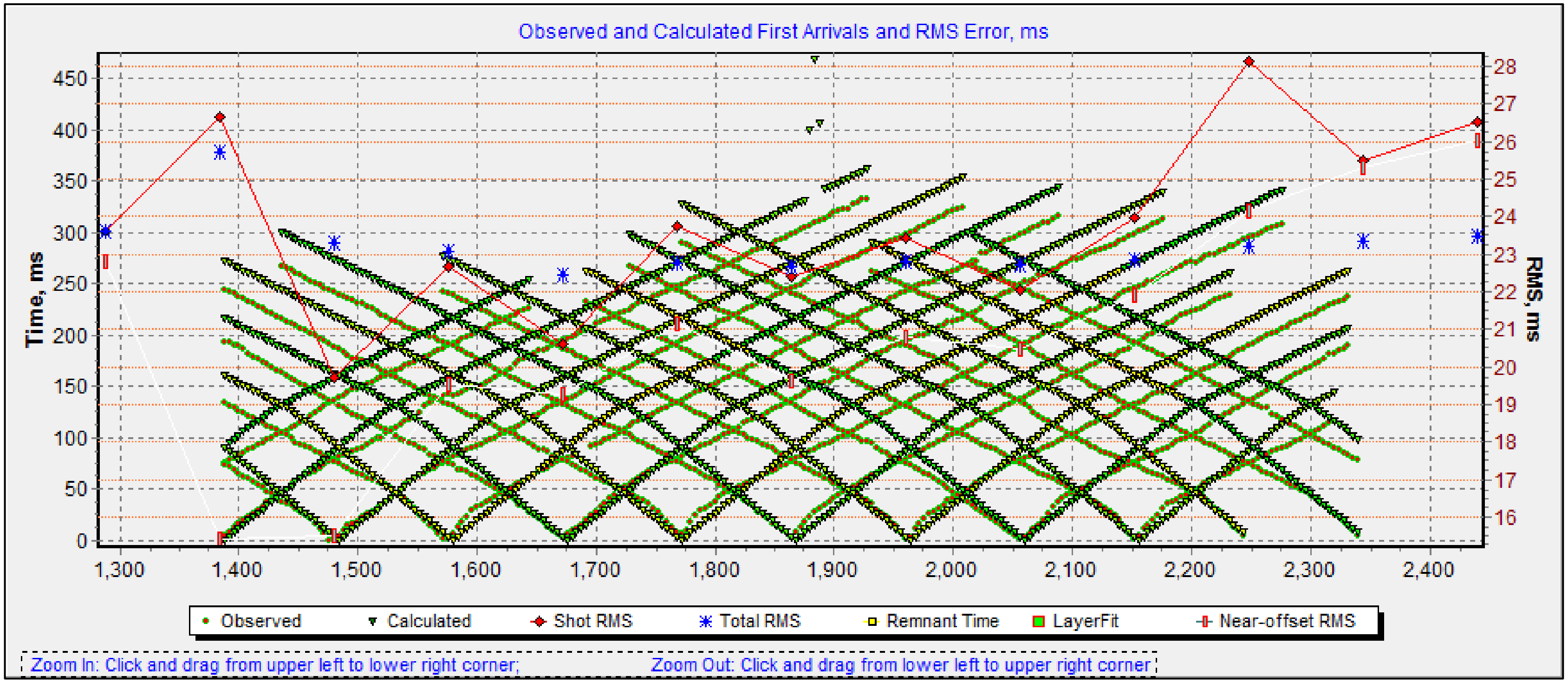

Figure 26: This figure illustrates the difference between calculated and observed first arrivals from the initial model derived from the MASW results. Though the trends are similar, there is still 24 ms RMS error between the observed and calculated first arrivals.

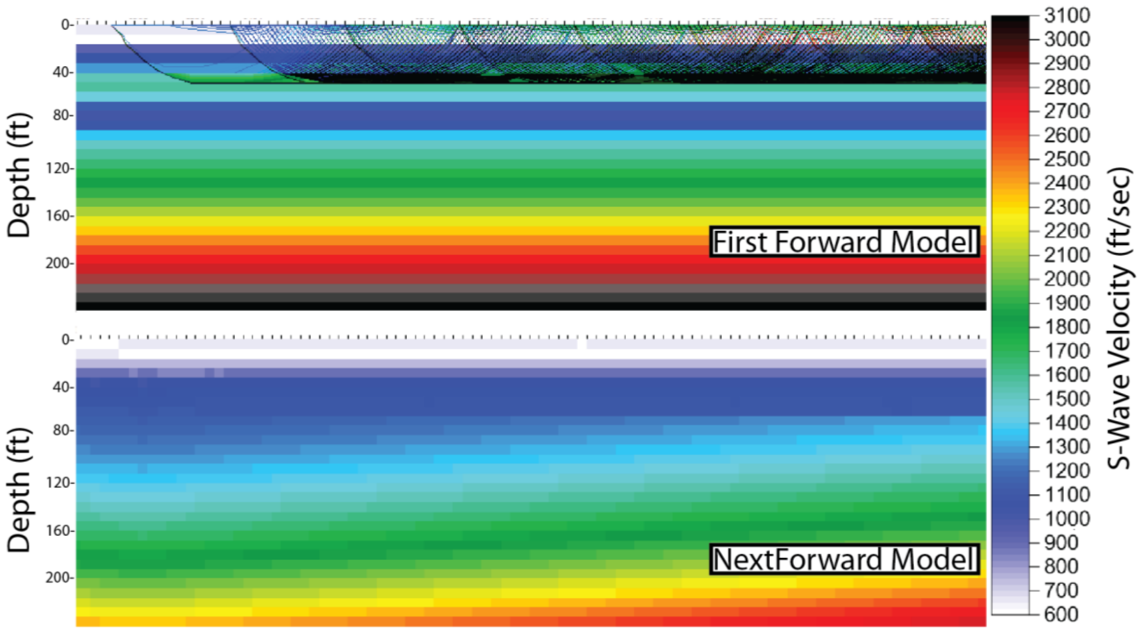

Figure 27: The ray tracing portion of the first forward model uses the MASW results. The computed ray paths representing the calculated first arrivals do not penetrate the low-velocity layer located at 56 ft depth. This yields calculated first arrivals very similar to the refraction-based initial model because the ray paths are similar. Upon the next iteration, the low-velocity layer is smoothed away, and the inversion proceeds with a velocity-gradient model.

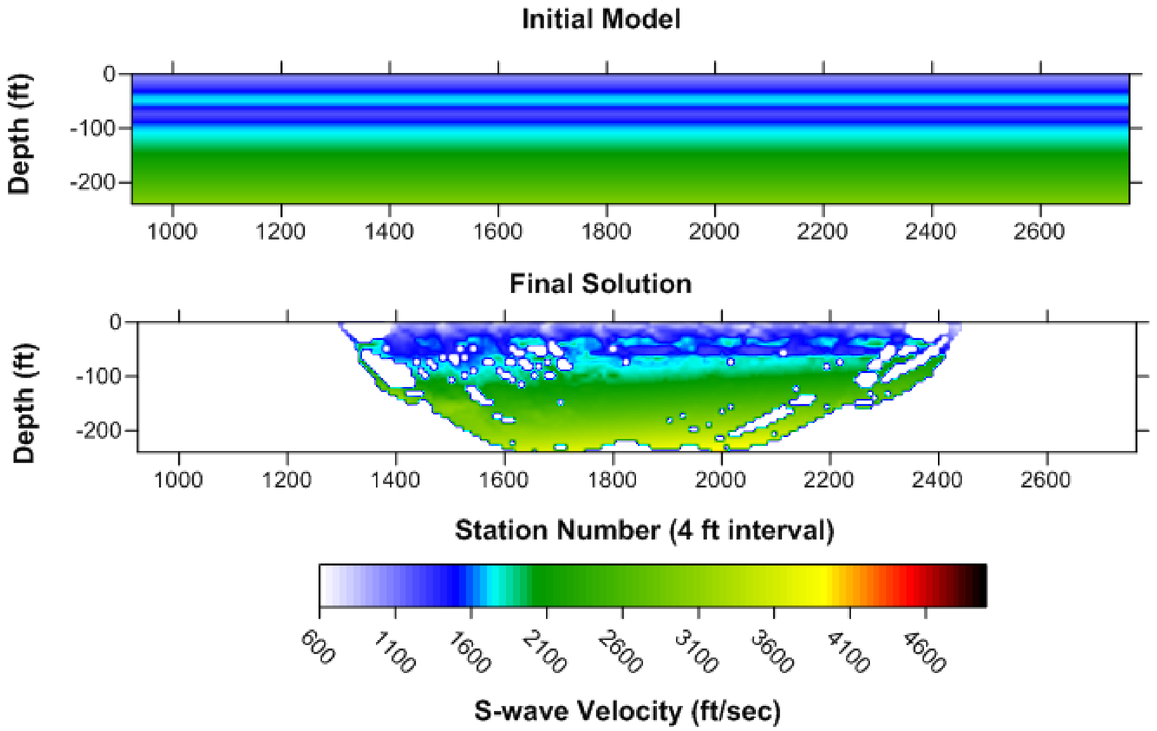

Figure 28: The solution for the initial model based on MASW results. The high velocity layer beginning at 40 ft has been highly distorted.

Results

Seismic tomography is a powerful tool, though construction of the initial model at this site is largely dependant on *a priori* information and the final solution must be geologically reasonable. During the iterative process of manipulating damping and smoothing parameters to converge on a solution, it is easy to steer the inversion towards a solution that is far from the true solution. The interpreter's influence can affect every step from picking the first arrivals to the final solution produced.

The best initial-model approximation is the refraction model. Based on the geology of the site, a linear velocity gradient was expected to provide a better approximation of the velocity structure than the refraction model. However, once the tomographic inversion began, the sharp velocity contrast became diffuse as a result of the defined smoothing constraints (Figure 23). The linear velocity function was more difficult to match to the distinctly linear first-arrival patterns, but the inversion process converged on a solution similar to that of the refraction model.

Downhole Survey

Introduction

Generally, surface geophysical methods are employed as a way to examine subsurface geologic structures and material properties while avoiding the environmental and financial costs of widespread invasive testing. Physical properties measured using surface geophysical methods can be verified or calibrated using borehole measurements. A downhole seismic survey allows direct measurements of travel times from a source at the surface to a geophone at depth in a borehole. Average and interval velocities can be calculated for materials surrounding the borehole (Sheriff, 1991). Compared to crosshole surveys, attenuation and natural filtering of the near-surface earth can significantly alter the characteristics of the first arrival from trace to trace, and more significantly from one borehole location to another. However, the near vertical ray paths of a downhole survey nearly eliminate the issues related to refracted first arrivals from a relatively fast layer.

Data Acquisition

A Geostuff brand three-component downhole 10 Hz geophone with a mechanical locking mechanism was used as the receiver for the downhole survey (Figure 29), the seismograph was a Geometrics Geode, and the source was a 16 lb sledgehammer striking a shear block and a steel plate. The geophone was lowered into the borehole down to 95 ft in well FT7 and 100 ft in well FT13. Once all of the shots were completed at each depth, the receiver was then raised one 5 ft interval to the next receiver depth. The cable was given slack once the geophone was locked into place to reduce noise traveling through the cable to the geophone (Hardage, 1983).

Figure 29: Image of the Geostuff brand three-component downhole geophone (10 Hz) with Kevlar cable and controller used for this survey.

At each depth the sledgehammer struck a steel plate with a vertical swing to generate P-waves, and then struck each side of the shear block to generate S-waves with opposite polarities. Each shot was repeated until the plate or shear block had adequate coupling to produce a high-quality first arrival. Most of the S-wave first arrivals would not have been identifiable without the recording first arrivals with opposite polarity to compare to (Figure 30).

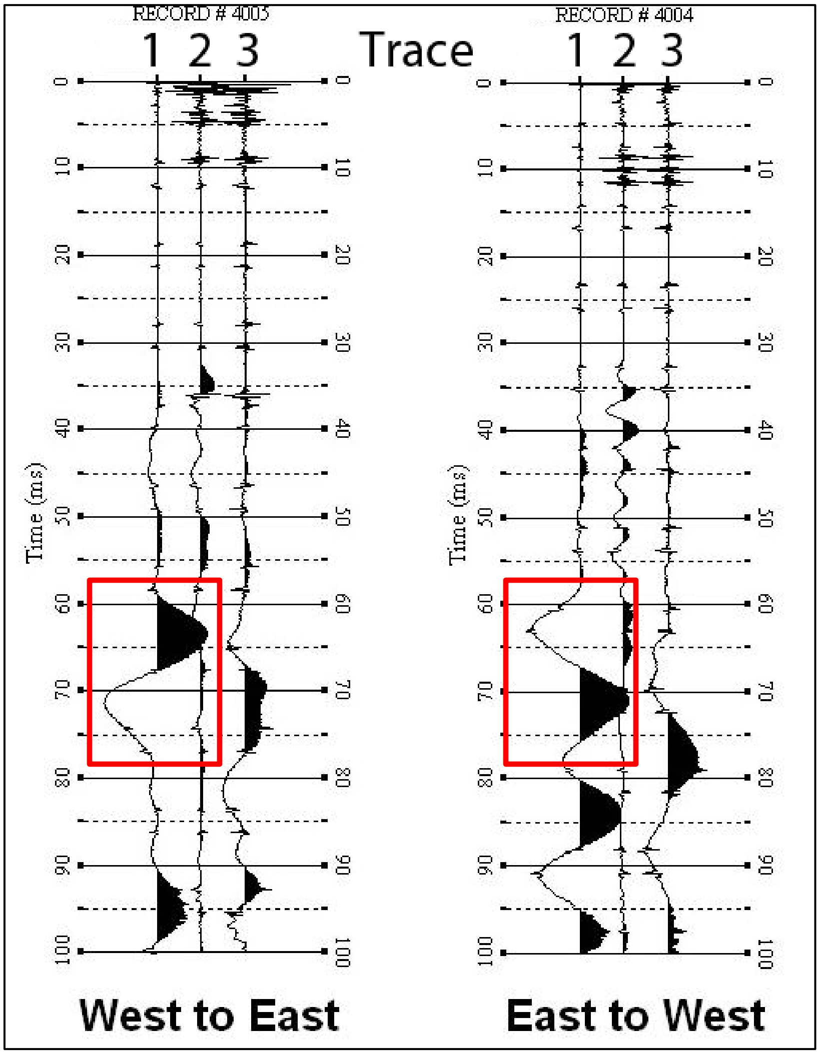

Figure 30: Example of two shot records from the same location where hammer swings struck opposite ends of the shear block. The large signal and wavelets of opposing polarity in channel one at 59 ms suggest that this is the S-wave first arrival.

Data Processing

In an ideal downhole S-wave survey, one of the horizontal components of the downhole geophone should be aligned parallel to the shear block to sample the maximum amount S-wave energy propagating this way. This alignment provides for easier interpretation and eliminates problems caused by anisotropy (Crice, 2011). However, if the geophone is allowed to rotate freely in the borehole over the course of a survey it is difficult to know the orientation of the geophone relative to the shear block without vector analysis of the shot record in the field or reading a compass attached to the geophone. This survey was conducted without physically orienting the geophone. Fortunately the S-wave first arrivals were still sampled by both horizontal geophone components, even at oblique angles, and interpreted based on the reverse polarity test.

The first phase in processing the downhole dataset was to identify the S-wave arrivals. Through careful examination of each record, the filename, trace number, and source orientation were recorded for the clearest S-wave arrival at each depth. Due to the random orientation of the geophone, the most recognizable S-wave arrival was identified for each depth sampled using the reverse-polarity test (Figure 30). These values are displayed in tables 1 and 2. The creation of gathers is described in appendix A.

Geometries must be defined to calculate distances between the source and receiver accurately (Figure 31). Depths were recorded from the top of the borehole casing, which was 1.5 ft above the ground. Source locations were 10 ft away from each borehole. For deeper surveys, the difference between the measured depth (***z***) and the actual diagonal ray path from the source to the receiver (***d***) is negligible, but in the near surface the source offset is important to consider for shallower receiver locations. Using these parameters the recorded depths were converted into diagonal distances (Equation 8). The calculated values (Tables 3-6) were used in conjunction with first arrival picks to calculate average and interval velocities.

$$\boldsymbol{d = \sqrt{(z - 1.5\ \mathrm{ft})^2 + (10\ \mathrm{ft})^2}} \qquad \textbf{(8)}$$

The diagonal ray path (***d***) is the shortest distance between the source and the receiver. Theoretically the first arrival of a wavefront from the source should take this path to the receiver. Velocities were calculated for each depth using first arrival times for each trace. To accurately pick S-wave first arrivals, a substantial amount of gain was applied to the record, differentiating the onset of the first arrival from the background noise. To improve the consistency of the P-wave arrival picks, the pick was made at the first zero crossing of the wavelet. Then the average amount of time between the zero crossing and the true first break seen on traces with high signal-to-noise ratio was subtracted from that time. In this study the average time used was 4.5 ms. This method assumes the wavelet phase and frequency bandwidth does not change from trace to trace (Figure 32; Figure 33). The first arrivals were picked using this method because the first arrivals were indistinguishable from noise even with high gain applied.

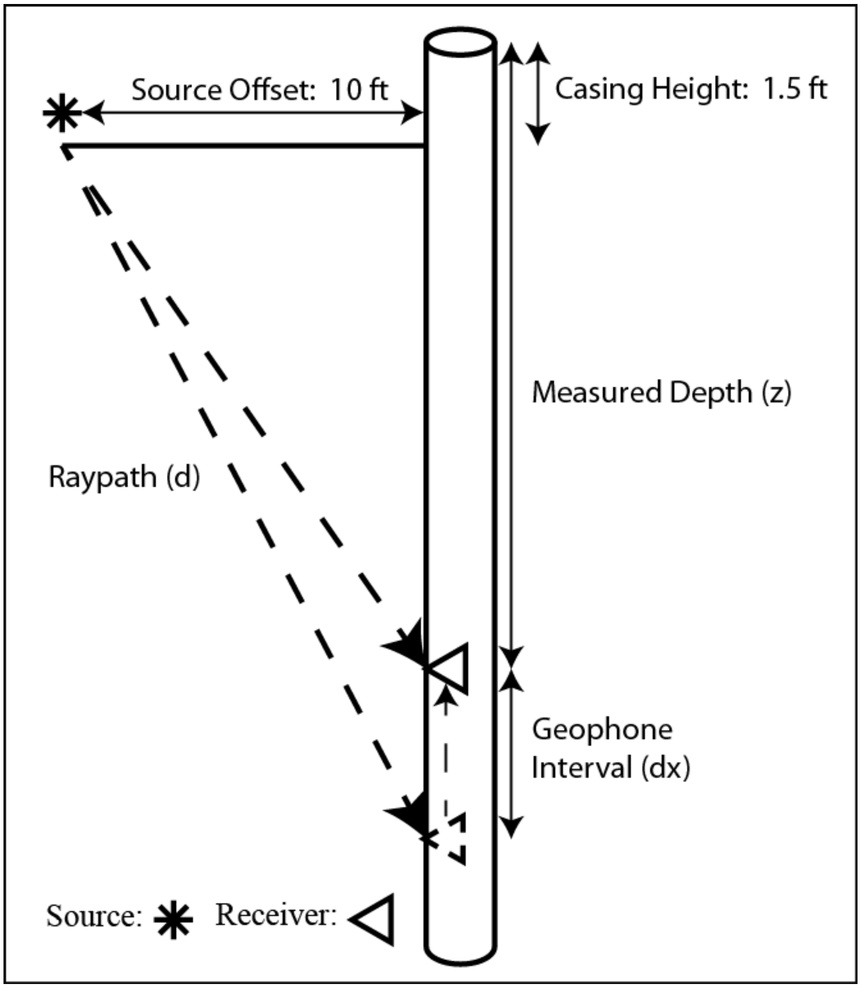

Figure 31: This figure depicts the geometric relationship among components of the downhole survey.

Results

Once first arrivals were picked, average (Figure 34) and interval velocities (Figure 35) were calculated (Tables 3-6). Average velocities were calculated using the picked arrival times as well as the distances between the source at the surface and the receiver in the borehole. Average velocity is the mean of all of the velocities of the material between the surface and the receiver depth. Interval velocity is the measure of material velocity between two receiver depths (Sheriff, 1991).

Several sources of error must be considered in borehole calculations. Sources of error in the time domain considered here include picking error, time break inconsistency, and sampling interval. Sources of error in depth measurements include measurement accuracy, cable stretch, and cable tightening. Also, in downhole S-wave gathers, the shape of the first-arrival wavelet phase seems to vary with depth. This changes the first break of the wavelet and must be factored in as a source of error.

A previous downhole study by the KGS used a geophone at the surface for quality control of the time break consistency showed an average error of about 1 ms. The sampling interval of the seismograph for the YPG downhole survey was 1/16th ms, giving an error of 1/16th ms which is insignificant relative to the other sources of error in the time domain. The geophone depth from the top of the borehole casing was estimated to possess an error of less than ¼ of an inch. Using a Kevlar cable with a relatively light geophone at depths shallower than 100 ft makes cable-stretch error negligible. Because relatively light geophones allow for a some cable tightening an error of of 1 inch of cable tightening at maximum depth was estimated. To estimate human error that might alter picks based on how the phase or signal quality of the first arrival from trace to trace, the maximum standard deviation of a set of 5 picks was factored into the error of each trace.

The P-wave data is of higher quality than the S-wave data. Between 80 and 100 ft, the shear-first arrival wavelet has a consistent phase and bandwidth, but at shallower depths the phase and frequency content of the wavelet varies and is difficult to pick consistently. This is the primary source of error for the S-wave data. No first arrivals were even picked for the S-wave data in well FT7 above 25 ft, these arrivals do not appear to represent the S-wave and are possibly the result of P-wave interference due to the oblique ray path from the source to receiver. However, both P and S-wave first-arrivals show a change in trends between 50 and 40 ft, suggesting a velocity inversion. P-wave arrivals from well FT13 show a change in wavelet characteristics between 50 and 70 ft which may result from sediment failing to backfill around the borehole casing (Hardage, 1983, pg 70). It is clearly evident from the change in P-wave and S-wave first-arrival trends that there is a velocity inversion around 50 ft.

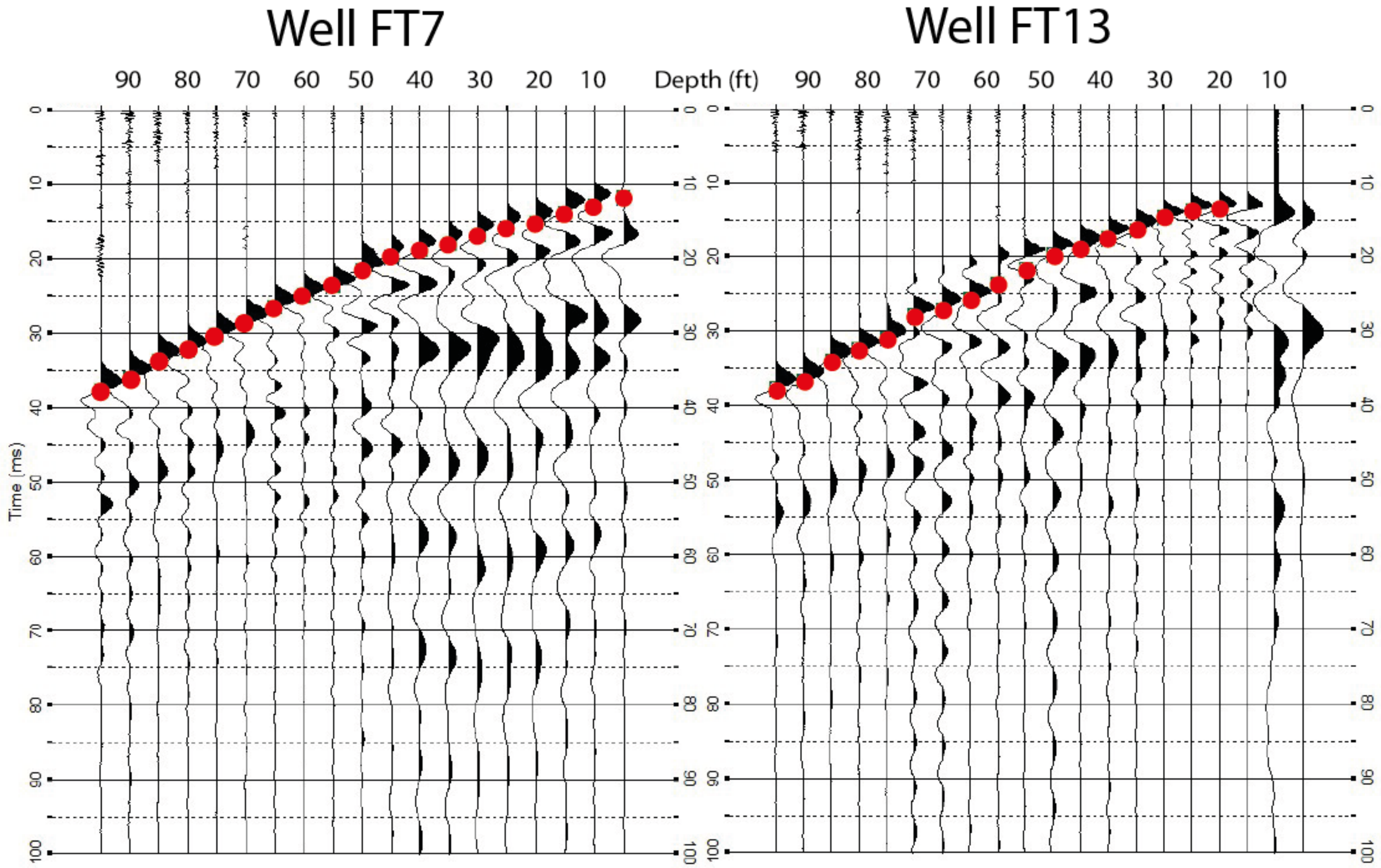

Figure 32: Collection of the downhole gathers for P-wave data from wells FT7 and FT13. Picks were made at the center of each red circle.

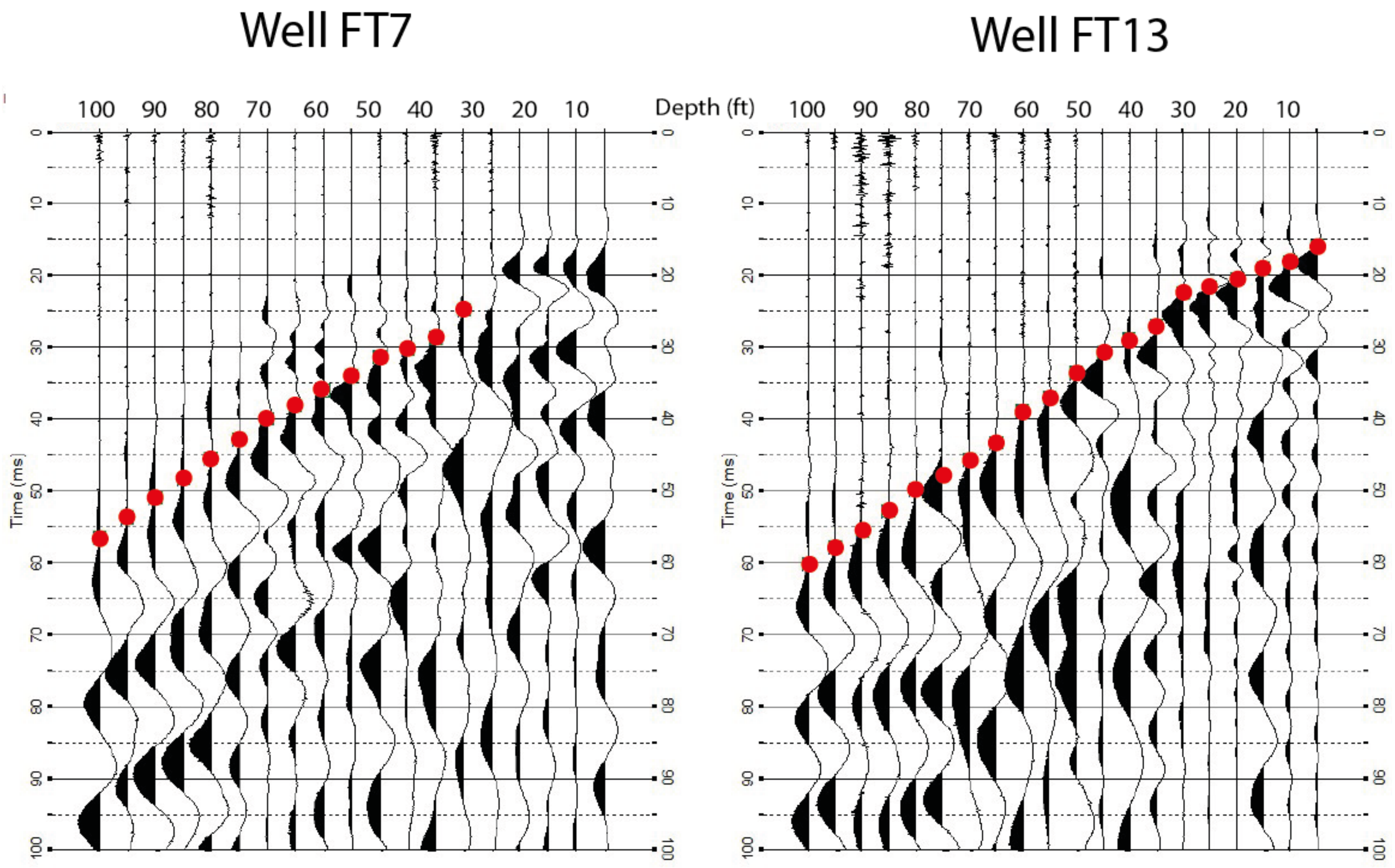

Figure 33: Collection of the downhole gathers for S-wave data from wells FT7 and FT13. Picks were made at the center of each red circle.

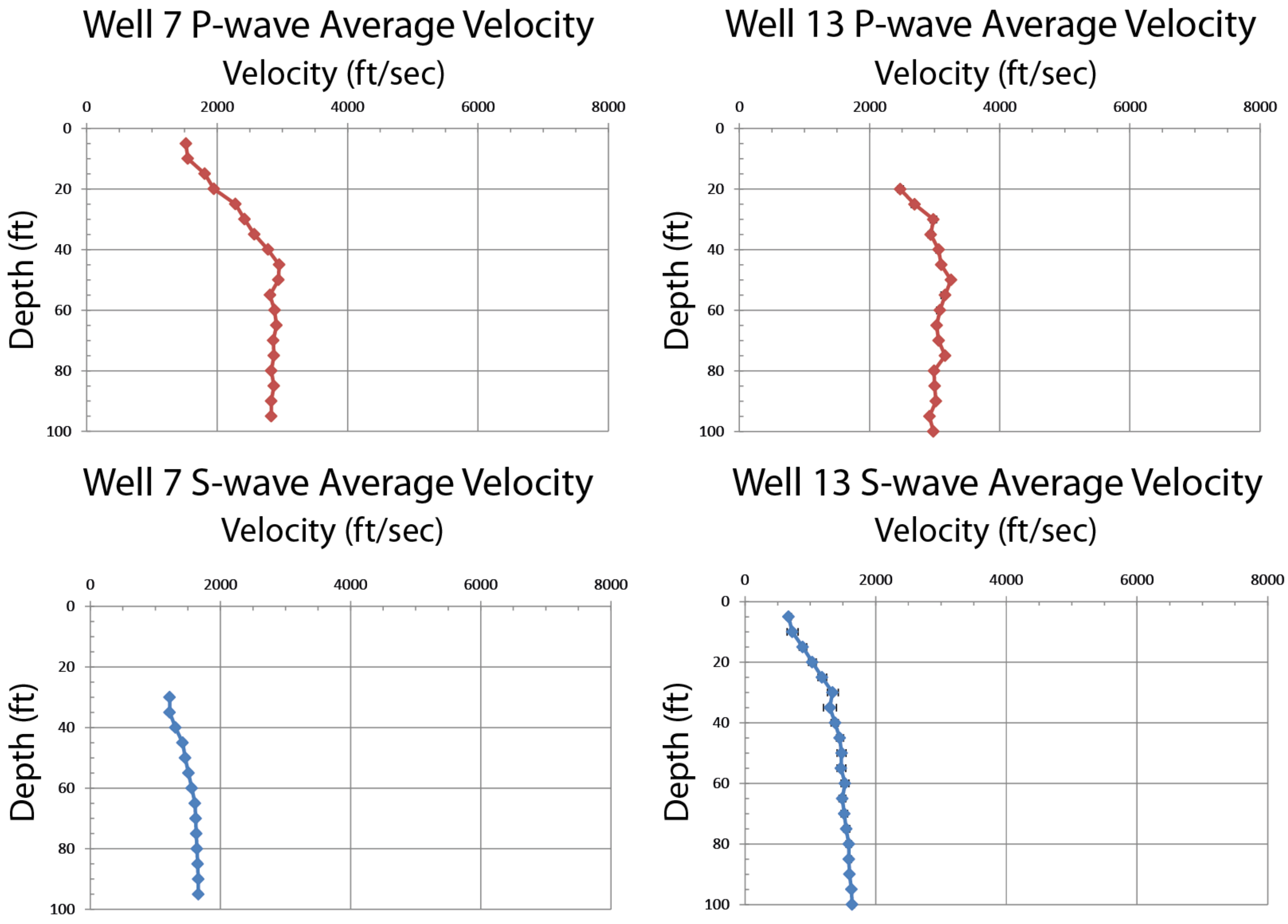

Figure 34: Average velocities calculated from first arrivals for both downhole surveys.

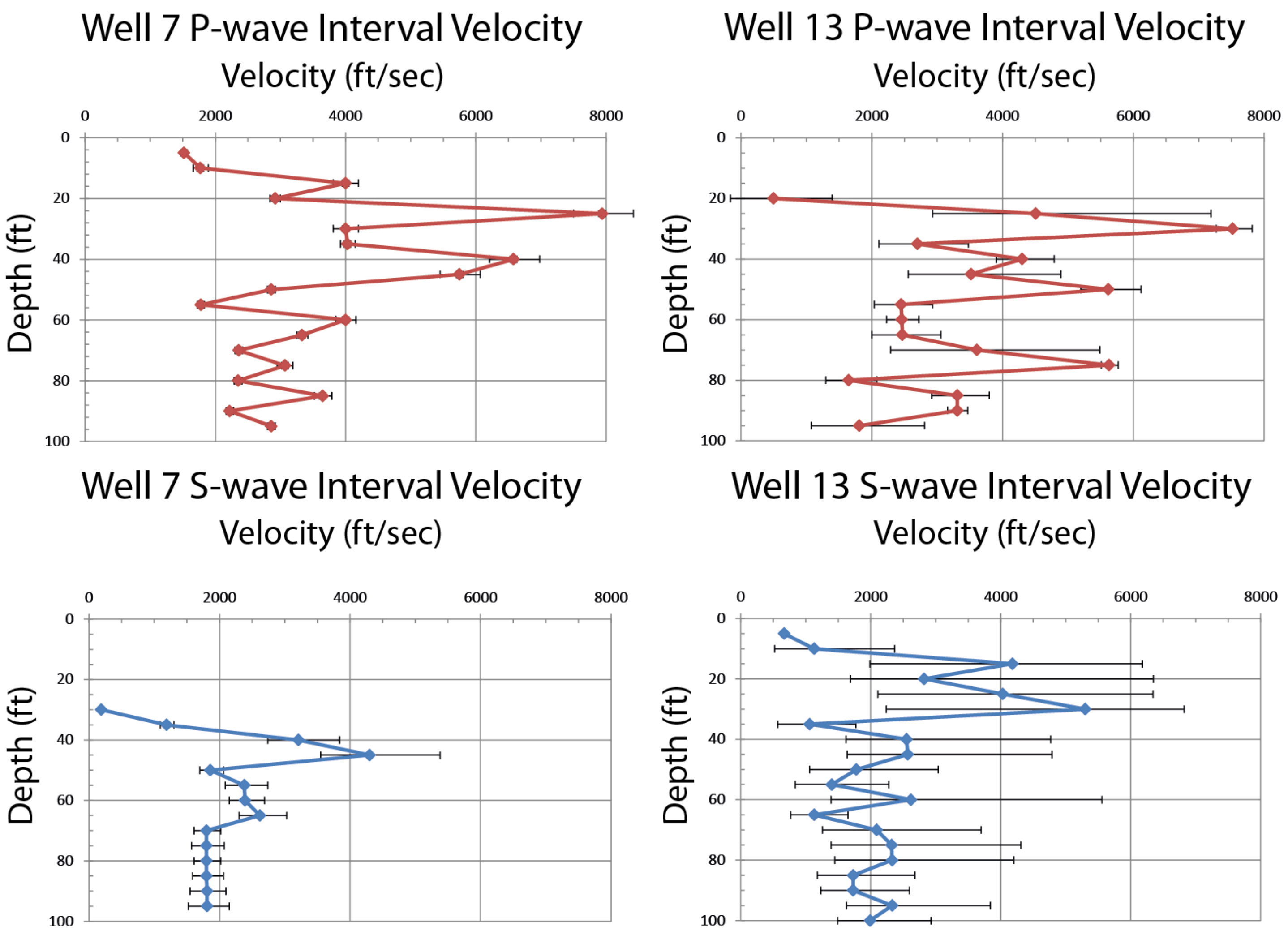

Figure 35: Interval velocities calculated from the average velocities in tables 3-6.

Tables

Table 1: Files determined to have the best representation of S-wave first arrivals for well FT7.

Measured Depth	File Used	Orientation of Shear block	Trace used
95	4002	SN	3
90	4008	NS	3
85	4018	NS	3
80	4026	NS	3
75	4030	NS	3
70	4039	NS	1
65	4043	NS	1
60	4052	NS	1
55	4056	NS	1
50	4069	WE	1
45	4072	NS	3
40	4085	EW	3
35	4092	SN	3
30	4104	NS	1
25	4115	SN	1
20	4122	NS	1
15	4126	NS	1
10	4135	NS	1
5	4139	NS	1

Table 2: Files determined to have the best representation of S-wave first arrivals for well FT13.

Measured Depth	File Used	Orientation of Shear block	Trace used
100	4145	NS	3
95	4150	NS	3
90	4154	NS	3
85	4160	NS	3
80	4168	WE	3
75	4172	NS	1
70	4177	SN	1
65	4181	EW	3
60	4188	EW	3
55	4195	EW	3
50	4202	EW	1
45	4205	NS	1
40	4219	WE	3
35	4223	NS	1
30	4230	EW	1
25	4236	WE	1
20	4240	EW	1
15	4243	NS	3
10	4250	WE	1
5	4254	EW	1

Table 3: P-wave velocities for well FT7.

Record	Pick (ms)	Depth (ft)	Total Distance (ft)	Average Velocity (ft/s)	Interval Velocity (ft/s)
4000	33.25	95	94	2860	2860
4006	31.5	90	89	2860	2220
4016	29.25	85	84	2910	3650
4024	27.88	80	79	2870	2350
4028	25.75	75	74	2910	3070
4037	24.12	70	69	2900	2360
4041	22	65	64	2950	3330
4050	20.5	60	59	2930	4000
4054	19.25	55	54	2860	1780
4061	17	50	50	2940	2860
4070	15.25	45	45	2950	5750
4079	14.38	40	40	2780	6580
4088	13.62	35	35	2570	4030
4093	12.38	30	30	2420	4000
4102	11.38	25	26	2200	7940
4111	10.75	20	21	1860	2920
4120	9.38	15	17	1600	4000
4133	8.38	10	13	1190	1770
	7.25	5	11	690	1520

Table 4: P-wave velocities for well FT13.

Record	Pick (ms)	Depth (ft)	Total Distance (ft)	Average Velocity (ft/s)	Interval Velocity (ft/s)
	33.25	100	99	3010	4970
4000	32.25	95	94	2950	1810
4006	29.5	90	89	3050	3310
4016	28	85	84	3040	3310
4024	26.5	80	79	3020	1650
4028	23.5	75	74	3190	5630
4037	22.62	70	69	3090	3610
4041	21.25	65	64	3060	2470
4050	19.25	60	59	3120	2460
4054	17.25	55	54	3190	2450
4061	15.25	50	50	3280	5620
4070	14.38	45	45	3130	3520
4079	13	40	40	3080	4300
4088	11.88	35	35	2950	2700
4093	10.12	30	30	2960	7520
4102	9.5	25	26	2630	4510
4111	8.5	20	21	2350	498
4120		15	17	No pick	No pick
4133		10	13	No pick	No pick
		5	11	No pick	No pick

Table 5: S-wave velocities for well FT7.

Pick (ms)	Depth (ft)	Total Distance (ft)	Average Velocity (ft/s)	Interval Velocity (ft/s)
56.5	95	94	1680	1810
53.75	90	89	1670	1810
51	85	84	1670	1800
48.25	80	79	1660	1800
45.5	75	74	1650	1800
42.75	70	69	1640	1800
40	65	64	1620	2620
38.12	60	59	1570	2390
36.06	55	54	1530	2380
34	50	50	1470	1860
31.38	45	45	1430	4300
30.25	40	40	1320	3210
28.75	35	35	1220	1190
24.75	30	30	1210	188
	25	26	No pick	No pick
	20	21	No pick	No pick
	15	17	No pick	No pick
	10	13	No pick	No pick
	5	11	No pick	No pick

Table 6: S-wave velocities for well FT13.

Pick (ms)	Depth (ft)	Total Distance (ft)	Average Velocity (ft/s)	Interval Velocity (ft/s)
60.25	100	99	1660	1990
57.75	95	94	1650	2330
55.62	90	89	1620	1730
52.75	85	84	1610	1730
49.88	80	79	1600	2330
47.75	75	74	1570	2320
45.62	70	69	1530	2090
43.25	65	64	1500	1130
38.88	60	59	1540	2620
37	55	54	1490	1400
33.5	50	50	1490	1780
30.75	45	45	1460	2570
28.86	40	40	1390	2550
26.97	35	35	1300	1060
22.5	30	30	1330	5300
21.62	25	26	1160	4030
20.5	20	21	976	2820
19	15	17	789	4180
18.12	10	13	552	1130
15.88	5	11	315	667

General Discussion

Each method compared in this study has inherent strengths and weaknesses. At this site within the YPG, The MASW method is able to image a low-velocity layer which S-wave tomography is incapable of doing. However, the higher frequencies necessary to image the shallowest 20 ft are dominated by higher-mode energy, while refraction and tomography is able to detect a large velocity contrast within the shallowest 10 ft.

The MASW results indicate that the S-wave velocity begins to decrease below 50 feet (Figure 18). The downhole survey results support the presence of a velocity inversion below 50 ft depth. The low-velocity layer is most clearly evidenced by the change in the average velocity trends to overall slower velocities at 50 ft (Figure 34). This change in the velocity trend is expressed in the downhole gathers (Figure 32; Figure 33), where the trend of first arrivals changes slope at approximately 50 ft depth on each gather. The interval velocities are much more sporadic and have much larger error bars, however, these measurements show a general velocity inversion beginning at about 50 feet (Figure 35).

According to the lithological sampling (Figure 6) The S-wave velocity inversion at 50 ft corresponds to an increase in clay content to over 80% consistently. This contradicts laboratory measurements indicating that V_P/V_S ratios should increase with clay content (Prasad *et al*., 2005). However the laboratory samples were created artificially, and the authors admit that further studies are necessary to determine the effects depositional fabrics may have on rock properties under near-surface conditions. For example, clay rich sediment deposited as part of a gravity flow event which are later dessicated may have different velocities than sediments with the same clay content deposited by fluvial events. More extensive P-wave velocity and anisotropy analysis may provide more insight into the true rock properties in this area.

Though MASW and downhole seismic provide valuable information at depth, site limitations make these measurements less convincing at the shallowest depths. The MASW method has limited resolution in the upper 20 ft due to dominant higher-mode energy above 30 Hz at this site. Downhole measurements shallower than 25 feet are the least representative of true geology. Above 25 ft the angle of incidence for arriving wavefronts exceeds 20 degrees. Also, the annular space between the borehole and the casing undergoes more mechanical deformation at shallower depths as material infilling occurs in unconsolidated sediment.

Refraction calculations gave evidence for a shallow velocity contrast between 800 ft/sec and 1700 ft/sec within the first 8 ft (Figure 22). Before the first round of tomographic inversion the model based on refraction analysis was already a viable solution with only 5 ms RMS error between calculated and measured first arrivals. The first arrival trends generated by the first round of the MASW-based model were very similar (Figure 26), but the 1700 ft/sec layer appeared to be too deep to match the measured first arrivals on the first iteration. The refraction-based solution had the least amount of error (4 ms) and the best ray coverage (Figure 23). Refraction analysis and refraction-based tomography provide more believable results at shallower depths than MASW or downhole seismic due to site-specific limitations.

The geology of the shallow subsurface at the YPG provides challenges for each of the geophysical methods tested in this study. Fortunately, the depths that each method is unable to resolve do not overlap. In situations where one method is weak, it makes sense to supplement that method with results from a method that is stronger in that situation. For this reason the best method for determining S-wave velocities for shallow unconsolidated sediment at the YPG involves a combination of MASW and refraction analysis. Refraction analysis provides the most accurate S-wave velocity estimation for the upper 20 ft, while MASW can accurately estimate S-wave velocities between 20 and 100 ft.

Shallow velocity contrasts and velocity reversals have been proven to excite higher modes in surface waves (O’Neill and Matuoka, 2005). If the velocity increase above 20 ft is correct, then it may be the reason that higher modes surface waves are so prevalent at YPG and MASW is unable to confidently resolve velocities at these depths. To test this, synthetic seismic data were created using two velocity models. A 2-layer model based solely on refraction analysis (Figure 36), and a 4 layer model based on a combination of refraction analysis and the velocity inversion estimated with MASW (Figure 37). The 2-layer model resembles the phase velocity trends and higher-mode energy content of real data (Figure 36). The addition of the velocity inversion detected with MASW adds details that more closely match the real dispersion image, such as lowered phase velocity at lower frequencies. Synthetic seismic models based on shallow velocity information from S-wave refraction analysis and deeper velocity information based on MASW create dispersion images that closely resemble data collected at YPG.

Conclusions

A number of geophysical methods was applied to the study area at the Yuma Proving Grounds to determine the best method for determining S-wave velocities of these shallow unconsolidated sediments. The methods considered in this paper are MASW, S-wave refraction tomography, and downhole seismic. The objectives of this study were to compare strengths and weaknesses of three different geophysical methods and determine the most accurate depiction of S-wave velocities in the subsurface.

The MASW inversion of the fundamental mode consistently provided evidence of a velocity inversion beginning around 50 ft into the subsurface that is confirmed by downhole seismic analysis. MASW was also able to image what might be a paleo-channel within the low-velocity layer. The MASW method at this site displays a higher mode with a significant amount of energy. A shallow velocity contrast may be exciting higher mode Rayleigh waves.

While both methods generally agree on the range of velocities in the upper 50 ft of material, the MASW method shows uncertainty in the upper 20 ft is where the greatest uncertainty for the MASW method lies due to the overwhelming energy of the higher mode. S-wave refraction indicates that the S-wave velocity increases from 800 ft/sec to 1700 ft/sec within the first 8 ft, but cannot successfully resolve low-velocity layers. In this case the best course of action is to supplement areas where one method is weak with another method’s strengths. The most accurate measurement of S-wave velocities in shallow unconsolidated sediments at the YPG site is achieved by combining the shallow velocity information provided by refraction tomography with the deeper velocities calculated through MASW.

Appendix A: Creation of Downhole Gathers

This appendix describes the method by which the raw downhole data were reorganized into P and S-wave gathers using the KGS software. There was no software platform developed at the KGS specifically for processing borehole data, the method described here was developed under the guidance of Shelby Peterie, a geophysicist employed at the KGS.

First, extract each trace selected in tables 1 and 2 and re-sort them into a single gather. All of the processing in this project was done with KGS software which uses a standardized KGS data format. The header words used in the KGS format record geometric-location variables such as trace number, file number, and station number. Beginning with the earliest record with a desirable S-wave arrival (tables 1-2), the selected trace was cut from the original file and placed in a new master file using KGS SeisUtilities. Then the next record was opened and the chosen trace was cut and appended to the master file. This process was repeated for each record in the tables created during the selection process.

Once the master file was created, the header words had to be manipulated to view the traces in a single window. To do this, the WinSeis module “trhdchng.exe” was used to change the last trace flag to 0 (header word 88) and the source sequence number to 2, an arbitrary number (header word 92). The source sequence number is the only digital record of the file number, making notes such as tables 1 and 2 vital for recording the traces and file numbers used in this process.

Appendix B: Synthetic Modeling

To investigate the validity of the velocities estimated by the methods tested in this study, a couple of models were created to generate synthetic seismic data for comparison with data collected at the YPG. Dispersion images created for MASW analysis demonstrate that surface-wave energy at the YPG site is transferred to successively higher modes at increasing frequencies. It has been shown that higher-mode energy dominates the surface wave at sites with large stiffness contrasts and/or velocity reversals (O'Neill and Matsuoka, 2005). Both of the geophysical methods tested in this study suggest that these conditions exist at the YPG site. These models were created to compare the effects the estimated velocity structures have on surface wave modal energy partitioning.

The 2-layer model was created using P and S-wave velocities calculated through refraction analysis. This places a velocity contrast 10 ft deep, followed by a homogenous half space (Figure 36). When the synthetic seismic data is viewed in the phase velocity, frequency domain, higher-mode energy is excited for frequencies above 35 Hz. The same frequency range in the dispersion image from real data shows higher-mode energy with similar phase velocities (Figure 36). The shallow velocity contrast indicated by refraction analysis seems to be responsible for the higher mode surface-wave energy that is prevalent at this site.

A 4-layer model (Figure 37) was created by combining the shallow velocity contrast indicated by the refraction method with the low-velocity layer shown by the MASW results and the downhole seismic. The reduced phase velocities between 10 and

15 Hz are a result of surface waves with these frequencies propagating through the lower velocity layer. The velocity structure in the 4-layer model also excites the second higher mode more than the 2-layer model.

The P and S wave velocities for these models were determined using refraction analysis, MASW results. These velocities yield Poisson's ratios that are anomalously low for unconsolidated material with such high clay content (Prasad *et al.*2005). More extensive velocity analysis would be beneficial to more accurately measure P and S-wave velocities for future modeling efforts. These velocities could then be used to create more elaborate modeled data in an effort to bring the modeled dispersion images closer to the measured dispersion images. However, the velocity structures used to create the synthetic data (Figure 36; Figure 37) generate dispersion images with phase velocities and modal energy partitioning similar to dispersion images created using real data from YPG (Figure 36).

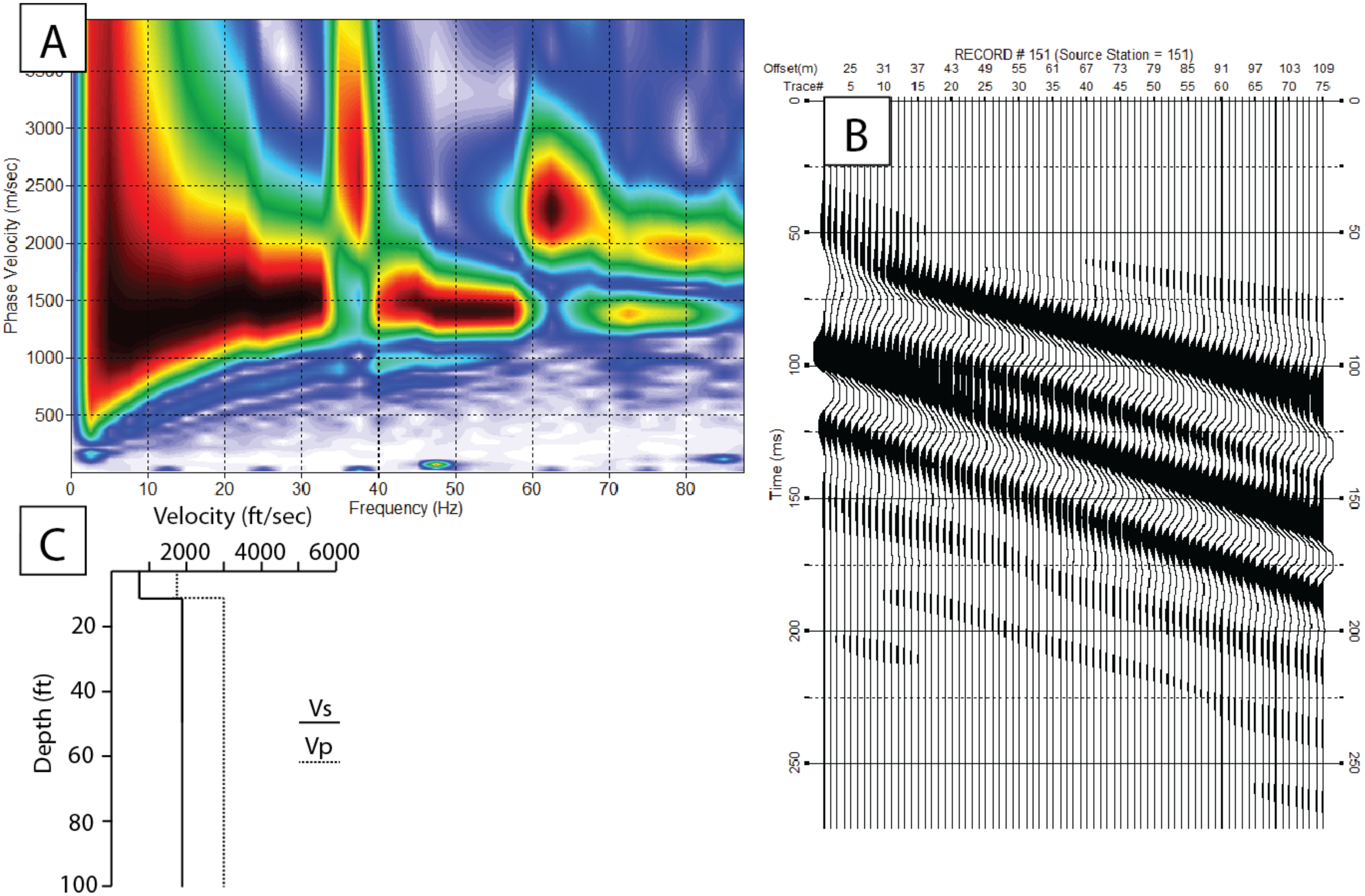

Figure 36: Dispersion image (A) generated from a synthetic shot gather (B). The data was generated using a 2 layer model (C). The abundance of higher-mode energy may be the result of the shallow velocity contrast modeled here.

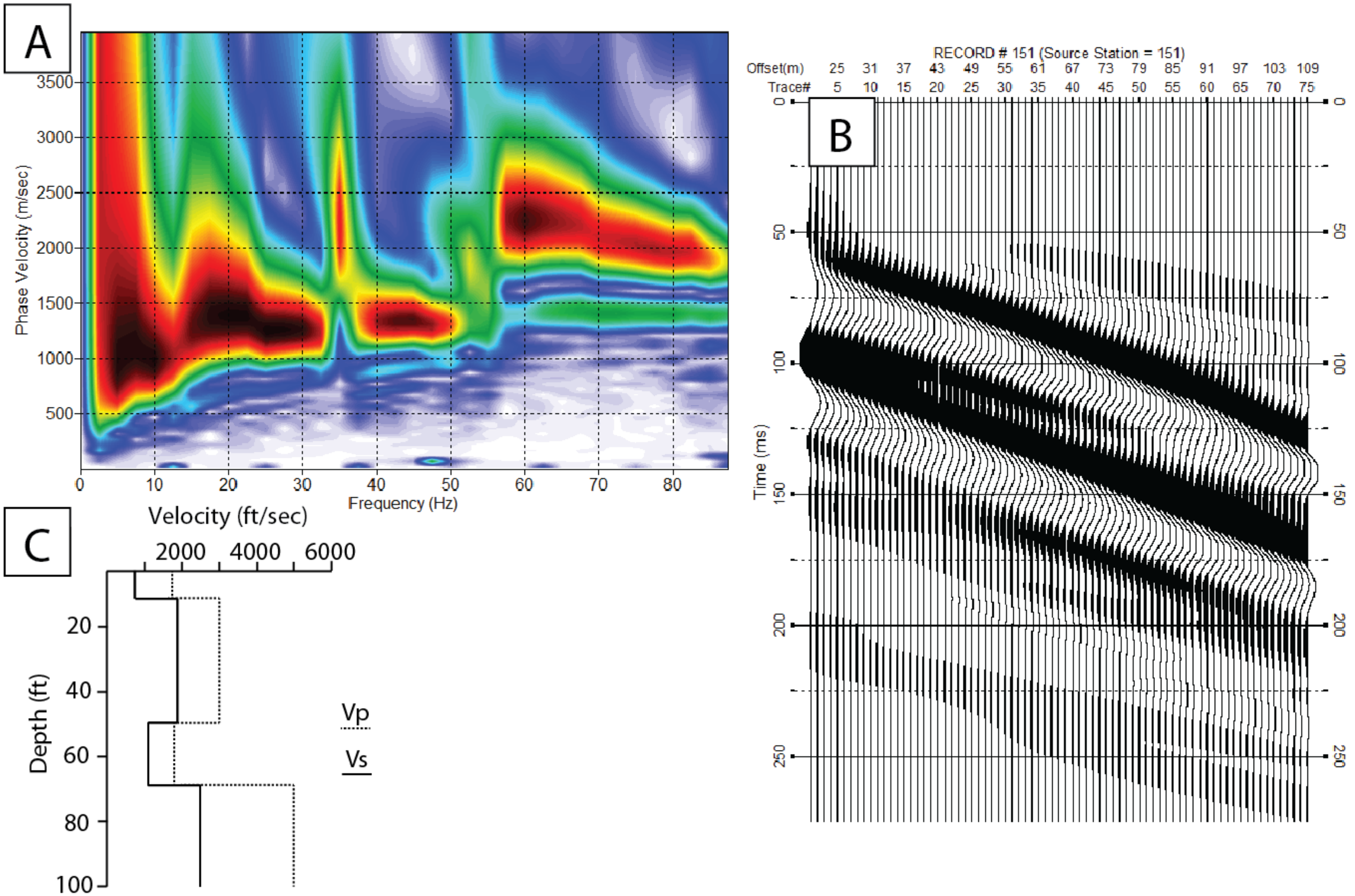

Figure 37: Dispersion image (A) generated from a synthetic shot gather (B). The data was generated using a 4 layer model (C). Notice the increase in energy in the highest visible mode when compared to the previous model (Figure 36).

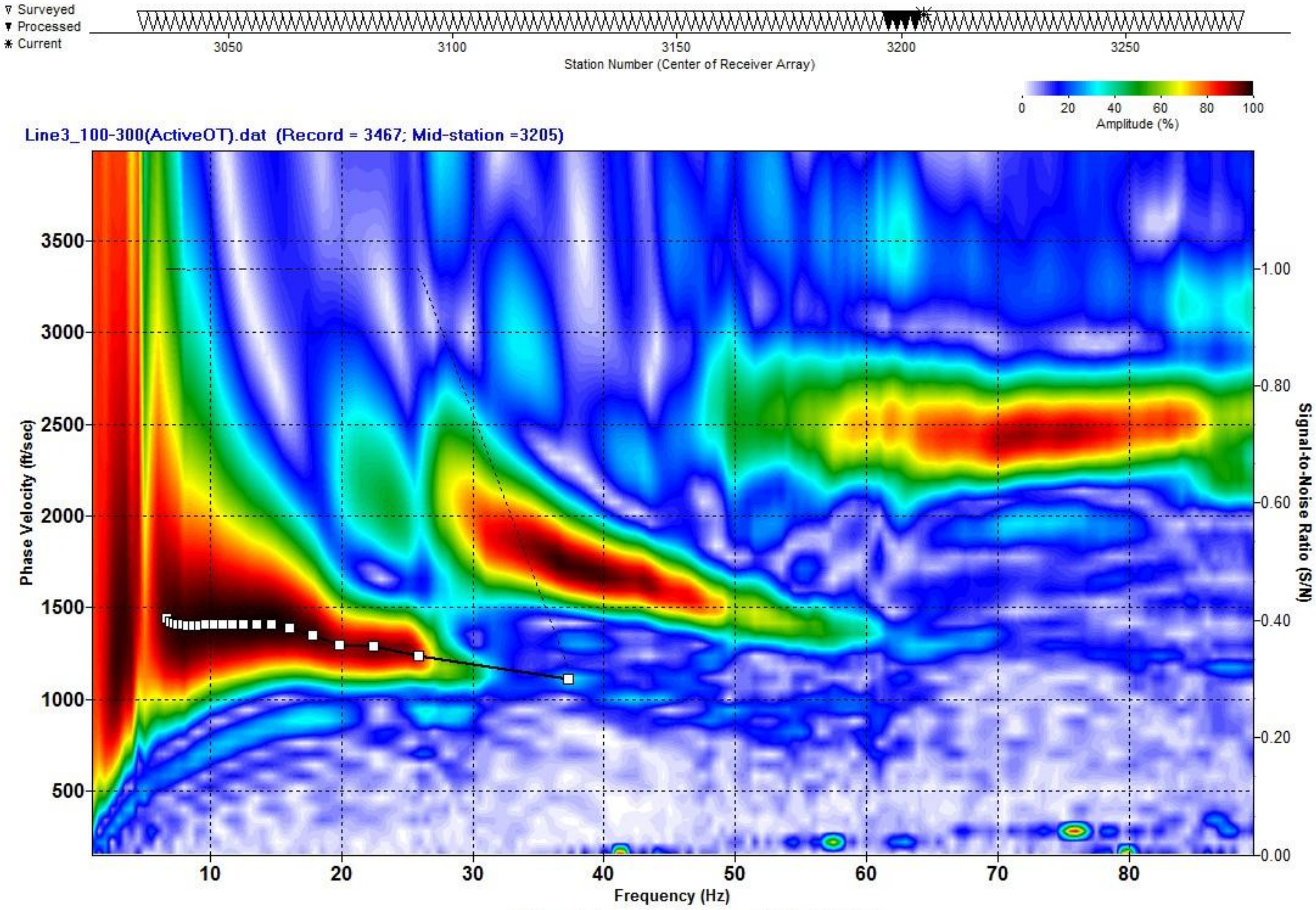

Figure 36: Dispersion image generated from real data from line 3 for comparison with Figure 36 and Figure 37.

References

Anbazhagan, P., and T.G. Sithram, 2008, Mapping of Average Shear Wave Velocity for Bangalore Region: A Case Study: Journal of Environmental and Engineering Geophysics, **v. 13**, issue 2, 69-84.

Babuska, V., and Cara, M., 1991, Seismic anisotropy in the earth: Kluwer Academic Publishers.

Borcherdt, R. D., 1994, Estimates of site-dependent response spectra for design (methodology and justification): Earthquake Spectra, **10**, 617-653

Crice, D., 2011, Near-surface, downhole shear-wave surveys: A primer: The Leading Edge, **30**, 164-171.

Eberly, L. D., and T. B. Stanley Jr., 1978, Cenozoic stratigraphy and geologic history of southwestern Arizona: Geological Society of America Bulletin, **89**, 921-940.

Ewing, W. M., W. S. Jardetsky, and F. Press, 1957, Elastic waves in a layered media, McGraw-Hill.

Gabriels, P., R. Snieder, and G. Nolet, 1987, In situ measurements of shear-wave velocity in sediments with higher-mode Rayleigh waves: Geophysical Prospecting: **35**, 187-196.

Green, R., 1974, The seismic refraction method – a review: Geoexploration, **12**, issue 4, 259-284

Hardage, B. A., 1983, Vertical seismic profiling, part A: Principles: Geophysical Press.

Heisey, J. S., K. H. Stokoe II, W. R. Hudson, and A. H. Meyer, 1982, Determination of in situ shear-wave velocity from spectral analysis of surface waves: Research report No 256-2, Center for Transportation Research, The University of Texas at Austin, December, 277 p.

Helbig, K., 1986, Shear-waves—what they are and how they can be used: Geophysical Developments, **1**, 19-36. Society of Exploration Geophysicists, Tulsa, Oklahoma.

Hunter, J. A., R. A. Burns, R. L. Good, A. Pugin, and H. Crow, 2010, Near-surface geophysical techniques for geohazards investigations: Some Canadian examples: The Leading Edge, **29**, no. 8, 964-977.

Ivanov, J., R. D. Miller, N. Stimac, R. F. Ballard, J. B. Dunbar, and S. Smullen., 2006a, Time-lapse study of levees in southern New Mexico: SEG Expanded Abstracts, vol. 25.

Ivanov, J., R. D. Miller, J. Xia, D. Steeples, and C. B. Park., 2006b, Joint analysis of refractions with surface waves: An inverse solution to the refraction-traveltime problem: Geophysics, **71**, no. 6, R131-R138.

Ivanov, J., R. D. Miller, P. Lancombe, C. D. Johnson, J. S. Lane Jr., 2006c, Delineating a shallow fault zone and dipping bedrock strata using multichannel analysis of surface waves with a land streamer: Geophysics, **71**, no 5, A39-A42.

Ivanov, J., R. D. Miller, and G. Tsoflias, 2008, Some practical aspects of MASW analysis and processing: Symposium on the Application of Geophysics to Engineering and Environmental Problems (SAGEEP 2008), Philadelphia, Pennsylvania, April 6-10, 21, No. 1, 1186-1198.

Ivanov, J., R. D. Miller, S. Peterie, C. Zeng, J. Xia, T. Schwenk, 2011, Multi-channel analysis of surface waves (MASW) of models with high shear-wave velocity contrast: 81st Annual International Meeting, SEG, Expanded Abstracts, 1384-1390.

Kanli, A. I., 2008, Image reconstruction in seismic and medical tomography: Journal of Environmental & Engineering Geophysics, **13**, 85-97.

Kanli, A. I., 2009, Initial velocity model construction of seismic tomography in near-surface applications: Journal of Applied Geophysics, **67**, 52-62.

McDonald E. V., G. K. Dalldorf, and S. N. Bacon, 2009, Landforms and surface cover of U.S. Army Yuma Proving Ground, Desert Research Institute Report no. R44.

McMechan, G. A., and M. J. Yedlin, 1981, Analysis of dispersive wave by wave field transformation: Geophysics, **46**, 869-874.

Miller, R. D., J. Xia, C. B. Park, and J. M. Ivanov, 1999, Multichannel analysis of surface waves to map bedrock: The Leading Edge, **12**, 1392-1396.

Miller, R. D., S. D. Sloan, and S. L. Walters, 2009, Shear-wave seismic study above Vigindustries, Inc. legacy salt jugs in Hutchinson, Kansas. KGS Open-file report **2009-3**.

Miller, R. D., O. M. Metheney, J. M. Anderson, and A.R. Wedel, 2010, Study of unconsolidated sediments at joint tunnel test range (JTTR) on Yuma Proving Grounds, Arizona: Kansas Geological Survey Open File Report, **2010-1**.

Nolan, J. J., S. D. Sloan, S. W. Broadfoot, J. R. McKenna, and O. M. Metheny, 2011, Near-surface void identification using MASW and refraction tomography techniques: SEG Expanded Abstracts, **30**, 1401.

O'Neil, A., and T. Matsuoka, 2005, Dominant higher surface-wave modes and possible inversion pitfalls: Journal of Environmental and Engineering Geophysics, **10**, 185-201.

Palmer, D., 1981, An introduction to the generalized reciprocal method of seismic refraction interpretation: Geophysics, **46**, 1508-1518.

Park, C. B., R. D. Miller, J. Xia, 1999, Multichannel analysis of surface waves: Geophysics, **64**, 800-808.

Park, C. B., R.D. Miller, and J. Xia, 2001, Offset and resolution of dispersion curve in multichannel analysis of surface waves (MASW): Symposium on the application of geophysics to engineering and environmental problems, SAGEEP 2001.

Park, C. B., and Miller, R. D., 2005, Seismic characterization of wind turbine sites in Kansas by the MASW method: Kansas Geological Survey Open-file Report, 2005-23

Prasad, M., M. A. Zimmer, P. A. Berge, B. P. Bonner, 2005, Laboratory measurements of velocity and attenuation in sediments, *in* D. K. Butler, ed., Near Surface Geophysics: Investigations in Geophysics no. 13, 491-502.

Reading, H. G., ed., 1996, Sedimentary environments: Processes, facies and stratigraphy: Blackwell Publishing, 57-59.

Sheriff, R. E., Encyclopedic dictionary of exploration geophysics. 4th ed. Tulsa: Society of exploration Geophysicists, 1991, 115-116.

Sloan, S. D., S. L. Peterie, J. Ivanov, R. D. Miller, and J. R. McKenna, 2010, Void detection using near-surface seismic methods, *in* R. D. Miller, J. H. Bradford, K. Holliger, eds., Advances in near-surface seismology and ground penetrating radar: Geophysical Developments no. 15, 201-218.

Socco, L. V., D. Boiero, S. Foti, R Wisén, 2009, Laterally constrained inversion of ground roll from seismic reflection records: Geophysics, **74**, G35-G45.

Stokoe II, K. H., and Nazarian, S., 1983, Effectiveness of ground improvement from Spectral Analysis of Surface Waves: Proceeding of the Eighth European Conference on Soil Mechanics and Foundation Engineering, Helsinki, Finland.

Stewart, R. R., 1991, Exploration seismic tomography: fundamentals: Society of Exploration Geophysicists.

Stewart, R., 1990, Exploration seismic tomography: fundamentals: Course Notes Series, **3,** 1-4.

Steeples, D. W., 1998, *Near-Surface Seismology, A Short Course*, sponsored by the Soc. Of Exploration Geophysicists and the Near-Surface Geophysics Section of the SEG.

Vidale, J., 1988, Finite-difference calculation of travel-times: Bulletin of the Seismological Society of America, **78**, 2062.

Xia, J., R. D. Miller, and C. B. Park, 1999, Estimation of near-surface shear wave velocity by inversion of Rayleigh waves: Geophysics, **64**, 691–700.

Xia, J., C. Chen, G. Tian, R. D. Miller, J. Ivanov, 2005, Resolution of high-frequency Rayleigh-wave data: Journal of Environmental & Engineering Geophysics, **10**, issue 2, 99-110.

Xu, Y., J. Xia, and R.D. Miller, 2006, Quantitative estimation of minimum offset for multichannel surface-wave survey with actively exciting source: Journal of Applied Geophysics, **159**, 117-125.